Tunnelling and Underground Space Technology 155 (2025) 106163

Contents lists available at ScienceDirect

Tunnelling and Underground Space Technology incorporating Trenchless Technology Research

journal homepage: www.elsevier.com/locate/tust

# Effect of soil improvement on ground movements induced by conventional tunnelling

Luca Masini [*], Federico Bergamo [1], Sebastiano Rampello

*Department of Structural and Geotechnical Engineering, Sapienza University of Rome, Via Eudossiana 18, 00184 Rome, Italy*

ARTICLE INFO

*Keywords:*
Tunnel construction
Masonry structures
Soil-structure interaction
Soil non-linearity

ABSTRACT

Line C of Rome underground will cross the city from southeast to northwest, with a total length of about 25 km, passing through the historical city centre. This is a difficult environment due to many archaeological finds and pre-existing buildings of great historical value. Along stretch T3 of the line two conventional tunnels connect the TBMs launching pit to the new San Giovanni station. They run for a length of 140 m at a depth of about 25 m and reach the station passing at a short distance from the ancient Aurelian Walls (3rd century CE). Excavation of these tunnels was carried out following a three-stage procedure: (*i*) excavation of two small diameter tunnels ($D = 3$ m) using a mini slurry shield machine; (*ii*) soil improvement via cement grouting using *tubes à manchettes* installed radially from the mini-tunnels; and (*iii*) conventional excavation of the two running tunnels in the improved soil. An extensive monitoring system was set to control ground movements induced throughout the excavation process.

This paper presents the displacement measured at the ground surface during the construction activities, highlighting the effects induced by grouting. The effectiveness of a protective barrier, made by a line of piles, in reducing the movements induced by tunnelling in the Aurelian Walls is also assessed. A 2D FE back-analysis is finally presented, showing that a satisfactory description of the observed behaviour can only be obtained by simulating the volume changes induced by the cement grouting.

## 1. Introduction

The development of underground infrastructures, such as new subways, or the extension of pre-existing ones, requires a careful inspection of the potential consequences on the surroundings. In the case of tunnelling in urban environments, the main issue is represented by the ground movements induced by the excavation stages with detrimental effects on the adjacent monuments or historical buildings.

Tunnelling and excavation of deep open pits in urban areas are inevitably accompanied by ground movements that require an accurate and reliable prediction in the design stage. Together with predicting the excavation-induced subsidence trough, it is necessary to define any mitigation measure or corrective action in case the extent of the ground movements may produce damage to the adjacent pre-existing structures.

The ground movements induced by tunnelling depend on a series of factors, including the tunnel diameter and depth, the excavation procedures, the strength and stiffness characteristics of the soil and the protection interventions adopted to mitigate tunnelling effects.

They can be reduced by active or passive protective interventions. The former either improve the mechanical characteristics of the soil or control the ground settlements during tunnelling, while the latter produce a favourable variation of the displacement field induced by tunnelling. Compensation grouting is an example of an active mitigation technique whose effectiveness in reducing ground movements has been shown by site investigations and laboratory tests (e.g.: Mair and Hight, 1994; Mair, 2008; Masini et al., 2012, 2014). When the structure lies to the side of the tunnel, passive protective barriers, consisting of bored piles or diaphragm walls, can be installed before tunnelling, between the tunnel and the structures for which damage must be prevented, providing restraint to ground movements (Bilotta and Taylor, 2005; Di Mariano et al. 2007; Bilotta, 2008; Katzenbach et al. 2013; Bai et al. 2014; Fantera et al., 2016; Losacco et al., 2019; Rampello et al., 2019; Franza et al., 2021; Masini and Rampello, 2021). In this respect, Fantera et al. (2016) and Rampello et al. (2019) carried out a parametric FE study for the rational design of passive embedded barriers, investigating the influence of several factors, including, among others, the barrier

* Corresponding author.
*E-mail address:* luca.masini@uniroma1.it (L. Masini).
[1] Present address: Italferr S.p.A, Via V. G. Galati 71, 00155 Rome, Italy.

https://doi.org/10.1016/j.tust.2024.106163
Received 6 June 2024; Received in revised form 17 September 2024; Accepted 25 October 2024
Available online 1 November 2024

location and its embedment length, the barrier type (continuous or discontinuous), and the soil-barrier interface.

Additional interventions include soil improvement by cement grouting, which increases the shear strength and reduces the permeability of the treated soil. Cement grouting can be carried out using a variety of injection methods, including low-pressure permeation injections or the high-pressure jet-grouting technique (Rawlings et al., 2000). The former, also known as "impregnation injections" or "clogging", replaces the pore water with a chemical-cement mixture, without causing disturbance to the soil structure. The second one injects cement mixtures at very high pressures, forming columns of concrete and soil that contribute to increasing the strength and the stiffness of the treated soil (Croce et al., 2014).

Given the high value of the artistic and cultural heritage that characterises the historical centre of Rome, several active and passive mitigation techniques have been adopted in the project of the new Line C of Rome underground to mitigate tunnelling-induced effects and to prevent damage to the historical monuments potentially affected by the construction of the line.

This paper describes the displacement field monitored during the conventional excavation of two tunnels, about 140 m long, connecting the multifunctional pit 3.3 (Masini et al., 2020; Masini et al., 2021), which operates as a launch pit for the Earth Pressure Balance (EPB) Tunnelling Boring Machine (TBM) machines excavating the tunnels towards Amba Aradam station, and the new San Giovanni station. Tunnels construction followed a three-step procedure: two small-diameter tunnels (D = 3 m) were first excavated using a mini slurry-shield machine at a depth of about 25 m; then, soil improvement via cement grouting was carried out using tubes à manchettes installed in boreholes excavated radial to the bored tunnels. Tunnel construction was finally completed through the conventional excavation of the main tunnels, about 7 m wide, in the improved soil.

The northbound tunnel passes at a short distance (about 23.5 m) from the ancient Aurelian Walls at Porta Asinaria (3rd century CE); therefore, a protective barrier of adjacent piles, 0.8 m in diameter, was pre-installed close to the tunnel to protect the ancient city Wall.

The effectiveness of the adopted mitigation interventions is evaluated in the paper through the interpretation of the monitoring data and plane-strain numerical simulation of the excavation stages. This enabled the installation effects related to cement grouting to be recognised and described in the numerical analyses to reproduce the observed displacement field.

## 2. Project description

The stretch T3 of Line C of Rome underground extends from Piazzale Appio to Piazza Venezia, involving the construction of the Amba Aradam-Ipponio and the Fori Imperiali-Colosseum stations, as well as the excavation of two multifunctional pits, in Via Sannio and Piazza Celimontana.

The line consists of two single-track tunnels, with an outer diameter of 6.7 m, which were excavated at depths of 20 to 35 m from the ground surface using EPB-TBMs. However, for the short stretch at hand, connecting the San Giovanni station to the lunch pit 3.3 using the TBMs was not convenient due to the length of only about 140 m, and the tunnels were excavated adopting conventional excavation procedures, the northbound tunnel being located at a short distance (about 23.5 m) from the Aurelian Walls at Porta Asinaria.

The Aurelian Walls are part of the large defensive walls built by Emperor Aurelian between 270 and 275 CE. At Porta Asinaria they are in the proximity of the Basilica of San Giovanni, running approximately parallel to the northbound tunnel. The wall is 4 m thick and about 18 m tall from the foundation plane, with the foundation located 8–9 m below the current ground surface. The structure of the Aurelian Walls is made of combined tuff and brick masonry, with an inner core of poorly bonded tuff blocks. At an early age, the ground surface was at the same level on both sides of the walls. A backfill of anthropic origin, now about 10 m high, has accumulated on the side of the Basilica of San Giovanni since the medieval age, without any drainage system. This has caused outwards displacements of about 0.4 m at the top of the wall and development of diffused cracks along the masonry surface. Therefore, the primary concern was to prevent any detrimental effect induced by the excavation works on the ancient masonry structure.

To prevent any additional damage to the Aurelian Walls at Porta Asinaria, an embedded barrier made by adjacent piles of diameter D = 0.8 m, length L = 28 m, and spacing s = 1 m, was pre-installed at about 8.3 m from the axis of the northbound tunnel and 18.1 m apart from the ancient city wall. The horizontal extension of the barrier was 63 m (Fig. 1).

### 2.1. Instrumentation layout

A comprehensive monitoring system was installed along the stretch to control the effects induced by the excavation of the twin running tunnels. The system also provided an early warning in case any significant deviation from the predicted behaviour might require adjustment in the excavation sequences and/or the adoption of additional mitigation techniques.

Fig. 1 shows the layout of the monitoring system. Six arrays of instruments were set about normal to the tunnel axes, namely MOM 02–03-04–05-06–07. The instrumentation along the MOM alignments included settlement markers installed at the ground surface and vibrating-wire piezometer cells.

During excavation activities, wall movements were also monitored through precision levelling on displacement markers installed along the wall side facing the tunnels and by electric tiltmeters installed at wall mid-height to measure out-of-plane inclination.

### 2.2. Site conditions

Ground conditions close to the Aurelian Walls at Porta Asinaria are typical of the historical centre of Rome (Rampello et al., 2012; Masini et al., 2019). A detailed geotechnical investigation was carried out, involving site tests (CPT and Cross-Hole tests) and deep boreholes from which undisturbed samples were retrieved and tested in the laboratory. Fig. 2 depicts a cross-section taken at MOM-04 alignment, showing the ground conditions, the two tunnels, the protective barrier, the installed displacement markers and the piezometer cells. A 15 m-thick layer of made ground (MG) is first encountered from the ground surface (about + 35 m above sea level, a.s.l.), mainly consisting of coarse-grained material (sand and gravel); recent alluvial soils of the Tiber River of Pleistocene age are found underneath, extending down to a depth of 27 m (+8 m a.s.l.). The alluvia are variable in grading involving slightly overconsolidated clayey silt, sandy silt and silty sand (CS-SS); they overly a layer of sandy gravel of Pleistocene age (SG), with a thickness of about 15 m, from + 9.0 m to −6 m a.s.l., followed by a thick layer of stiff and overconsolidated silty clay, the blue Vatican clay of Pliocene age (OSC).

Soil parameters as obtained from in situ and laboratory tests are reported and discussed in detail in § 4.

Fig. 2 also shows the pore water pressure ($u$) measured by 4 vibrating wire piezometer cells (PE1P, PE1S, PE2S, PE2P) installed along the MOM-04 alignment. Values from the MOM-07 piezometers and those measured during the 2003 site investigation are also plotted in the figure. A constant hydraulic head H was observed in the made ground (H = 26.5 m a.s.l.) and in the deep layers of sandy gravel and stiff clay (H = 17.5 m a.s.l), with a downwards seepage in the intermediate silty soils. Such a condition is often encountered along line C of Rome underground and is induced by the pumping from the deep and permeable layer of sandy gravel for anthropic purposes.

The twin tunnels were excavated at depths of about 25 m from the ground surface, involving mostly the alluvial sandy silt. Therefore,

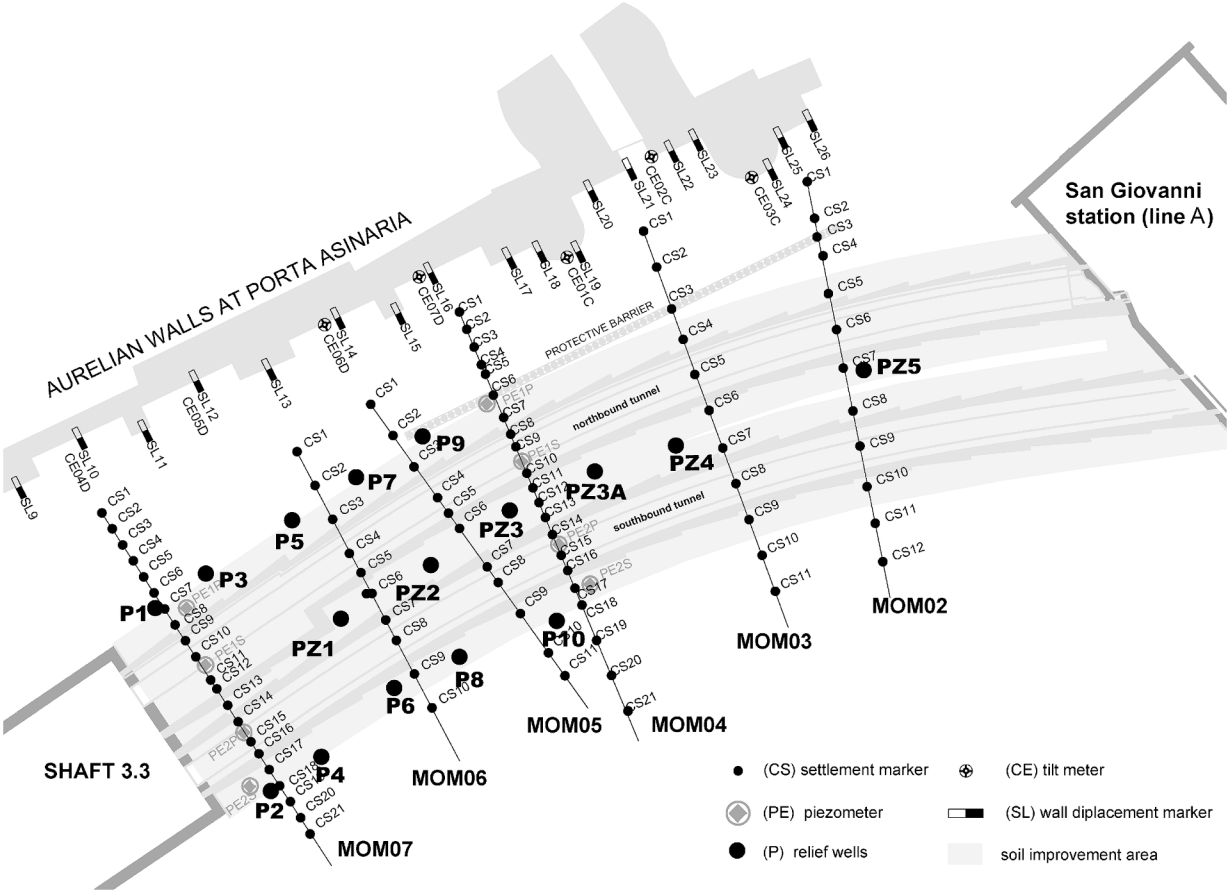


**Fig. 1.** Plan view of the monitoring system in the stretch between the TBM launching pit and *San Giovanni* Station.

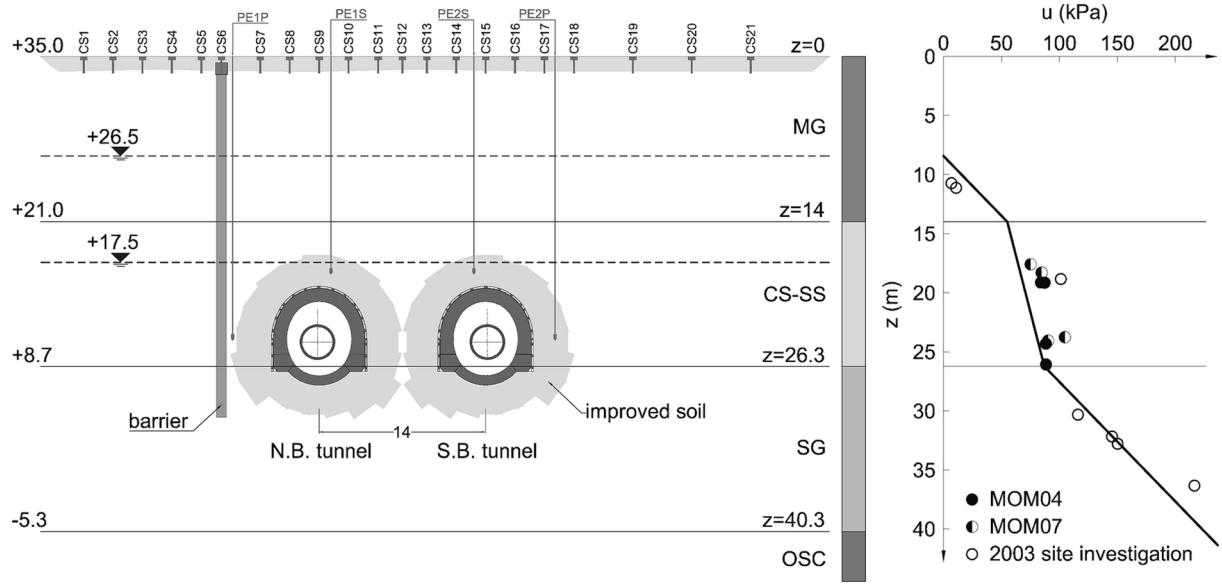


**Fig. 2.** Soil conditions and pore water pressure profile at the location of section MOM04.

tunnelling operations mainly involved the alluvia sandy silt (CS-SS) whose permeability was preliminary reduced via low-pressure cement grouting, as detailed in the following.

### 2.3. Construction sequences

The 140 m-long connection between the TBMs lunch pit 3.3 and *San Giovanni* station was excavated according to the following three stages: (*i*) two small-diameter tunnels (D = 3 m) were first excavated by a mini slurry shield boring machine at a depth of about 25 m (cover-to-

diameter ratio C/D = 7.8); (*ii*) soil improvement via cement grouting was carried out using *tubes à manchettes* installed in boreholes excavated radial to the bored tunnels; (*iii*) the main tunnels were excavated in the treated soil using the conventional method. Fig. 3 shows the main excavation sequences which will be detailed in the following sections.

#### 2.3.1. Mini tunnelling

The two mini-tunnels were excavated using a remote-controlled slurry shield boring machine with an outer diameter of 3.08 m. The excavated soil is collected into the excavation chamber and added with a water-bentonite mixture to form a slurry. The stabilisation of the tunnel face was obtained by keeping the slurry in the chamber to a pressure of 150–200 kPa higher than the pore water pressure at the excavation depth. The mini-TBM was advanced by the thrust transmitted to the lining made of precast concrete rings. The latter were pushed from a jacking station installed into the launching pit. An intermediate jacking station, about 40 m away from the TBM, reduced the thrust acting on the lining. The concrete rings of the lining have an outer diameter of 3 m, a thickness of 0.25 m and a length of 2.35 m; they were completely dismantled as the running tunnels were excavated.

The soil-lining gap was first filled with a water-bentonite mixture to reduce friction during lining jacking; then, after completion of the mini-tunnels, a cement grout was injected from the same valves used to inject the water-bentonite mixture.

#### 2.3.2. Soil improvements

At the end of the excavation of the two mini-tunnels, soil improvement was carried out in the layers of alluvial sandy silt (CS-SS) and sandy layer (SG), the latter found immediately underneath the tunnel invert (Fig. 2). Cement grouting was carried out at a pressure of 10–12 bar using tubes à manchettes installed in boreholes excavated radially to the bored tunnels. Twenty boreholes per cross-section were drilled using a longitudinal spacing of 0.6 m; the boreholes had a diameter of 80 mm, a length of 5–7 m, and a spacing of 18° in the radial direction.

Grout injections were performed through 50 mm-diameter PVC tubes, with 2 to 3 valves per meter. First, the soil-tube gap was filled using a water-cement grout with 8–10 % bentonite content and a water cement-ratio of 2–3 (32.5 grade cement). Then, soil improvement was obtained in two stages. A Mistrà-type cement grout (Table 1) was first injected with a 10–15 % bentonite content and a water-cement ratio of 2.5–3.5 (52.5 grade cement). The flowability of Mistrà cement grout was improved using chemical additives, which also reduced the pressure filtration that may lead to significant losses of water from the grout during injection, thus reducing the grout's capability of penetrating the soil (Masini et al., 2014). In the second stage, a chemical mixture of silica components (Litosil-type) was injected to obtain an additional reduction of the permeability of the treated soil.

**Table 1**
Grouts adopted for soil improvement.

| Grout properties | |
|---|---|
| *Mistrà type grout for injections* | |
| cement strength class | 52.5 |
| water/cement ratio | 2.5–3.5 |
| bentonite content (in weight of cement) | 10–15 % |
| Additive content (in weight of cement) | 0.2–0.4 % |
| *Litosil type chemical grout for injections* | |
| density | 1200–1500 Kg/m$^3$ |
| hardening time | 60–100 min |

#### 2.3.3. Conventional excavation of the running tunnels

The conventional excavation of the line tunnels was carried out in the improved soil by enlarging the mini-tunnels. Fan-like, overlapping pipe umbrellas, made of 114.7 mm-diameter steel pipes, were drilled and grouted at the crown, parallel to the direction of advancement of the excavation face. Each roof canopy is formed of 41 steel pipes, 12 m-long, enabling a maximum excavation span of 8 m. The full-face excavation of the tunnel was carried out along with the installation of the primary support 1 m away from the excavation face, which consists of IPN 160 steel ribs and 0.2 m-thick shotcrete. The final concrete lining, installed 35 m away from the excavation face, has a thickness of 0.8–1 m, a width of 6.72–7.72 m and a height of 7.70–8.20 m.

## 3. Field monitoring

Table 2 summarises the main stages of the construction activities and their duration. The mini tunnelling started from the southbound tunnel (Jan. 20, 2017) and it took about 27 days to complete. The northbound mini-tunnel tunnel was excavated in about 18 days (Mar. 13–31, 2017). Ground improvement activities started simultaneously from the inside of the two mini-tunnels. About 209 days were needed to complete the borehole drilling (June 27, 2017 to Jan. 22, 2018), while grout and

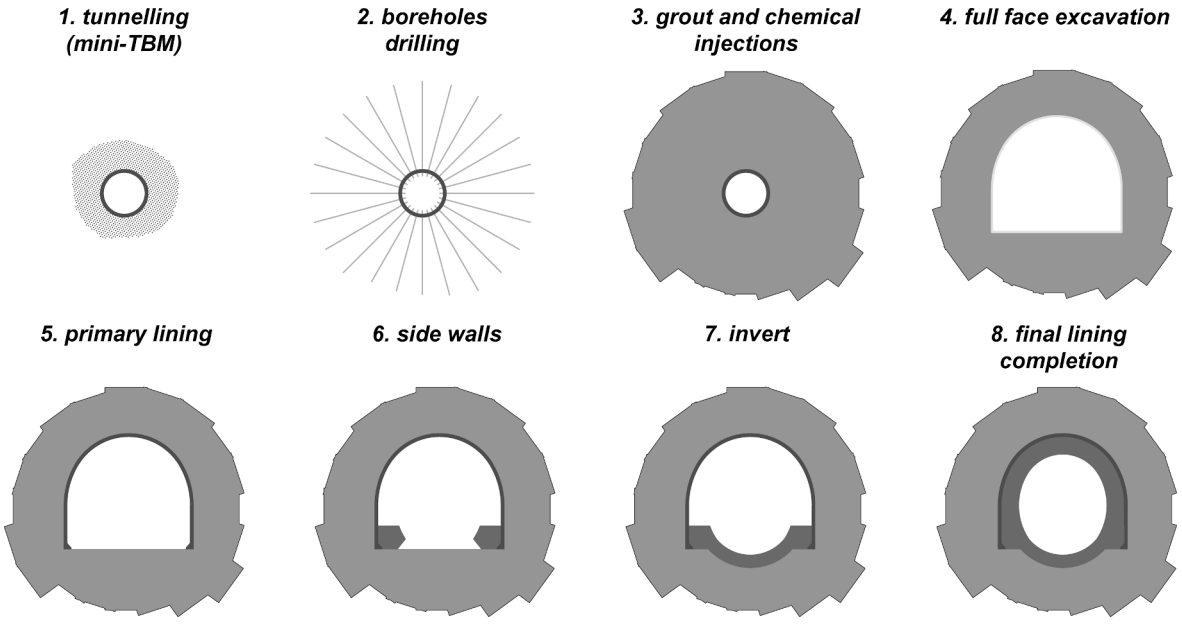


**Fig. 3.** Main excavation stages.

**Table 2**
Excavation sequences.

| construction stage | | start | end | Δt (days) |
|---|---|---|---|---|
| mini-tunnelling | southbound tunnel | 20/01/17 | 16/02/17 | 27 |
| | northbound tunnel | 13/03/17 | 31/03/17 | 18 |
| soil improvement | borehole drilling | 27/06/17 | 22/01/18 | 209 |
| | grouting injections | 23/01/18 | 19/10/18 | 269 |
| activation of relief wells | | from 20/11/18 | | |
| southbound running tunnel | | 15/11/18 | 07/07/19 | 234 |
| northbound running tunnel | | 26/04/19 | 21/10/19 | 178 |

chemical injections started the day after the end of borehole drilling and ended in 269 days (Oct. 19, 2018). The excavation of the southbound main tunnel was lengthy, taking approximately 234 days: this was because tunnel excavation had to be suspended just 5 days after the start of excavation (Nov. 20, 2018) due to a local collapse triggered by the basal heave of the improved soil at the tunnel spring line. Consequently, the excavation was suspended, and 16 relief wells were activated aside the tunnels layout, as shown in Fig. 1. The dewatering activities induced an average drawdown of the hydraulic head of about 9.5 m in the coarse-grained layer (SG), as detailed in the following section. Tunnelling activities were resumed about two months later (Jan. 18, 2019) and were completed on July 7, 2019. Excavation of the northbound tunnel took 178 days (Apr. 26 – Oct 21, 2019).

In the following, the vertical displacements measured by the settlement markers installed along the seven instrumented arrays are discussed for each excavation stage and the transversal displacement profiles are interpreted using the empirical relationships currently adopted in engineering practice (e.g.: Moh et al., 1996; O'Reilly and New 1982; Peck, 1969).

Fig. 4 shows the time histories of the vertical displacements measured at the monitoring sections MOM-04 and MOM-07: positive values indicate heaves. Measurements are referred to the readings taken about two months before beginning the excavation of the southbound mini-tunnel. Excavation of both mini-tunnels induced negligible settlements of about 3 mm at MOM-04 and 4 mm at MOM-07. During borehole drilling, the settlements are seen to increase gradually as the radial drilling approaches the instrumented sections, with a final value of about −13 mm and −8 mm at sections MOM-04 and MOM-07, respectively. In general, the settlements ascribed to borehole drilling were two to four times larger than those observed at the end of mini tunnelling. The grout injections caused an extensive heave, 60 % larger at section MOM-04 (about 154 mm) than that observed at section MOM-07 (96 mm). In the other monitoring alignments, the maximum heave ranged between 133 mm (section MOM-06) and 166 mm (section MOM-03). The variation in the observed heave might be ascribed to both soil conditions and the injected volume, which was not constant from borehole to borehole. Part of the observed heave was lost during the construction of the running tunnels because of the combined effect of the excavation activities and the drawdown from the relief wells in the deep layer of sandy gravel.

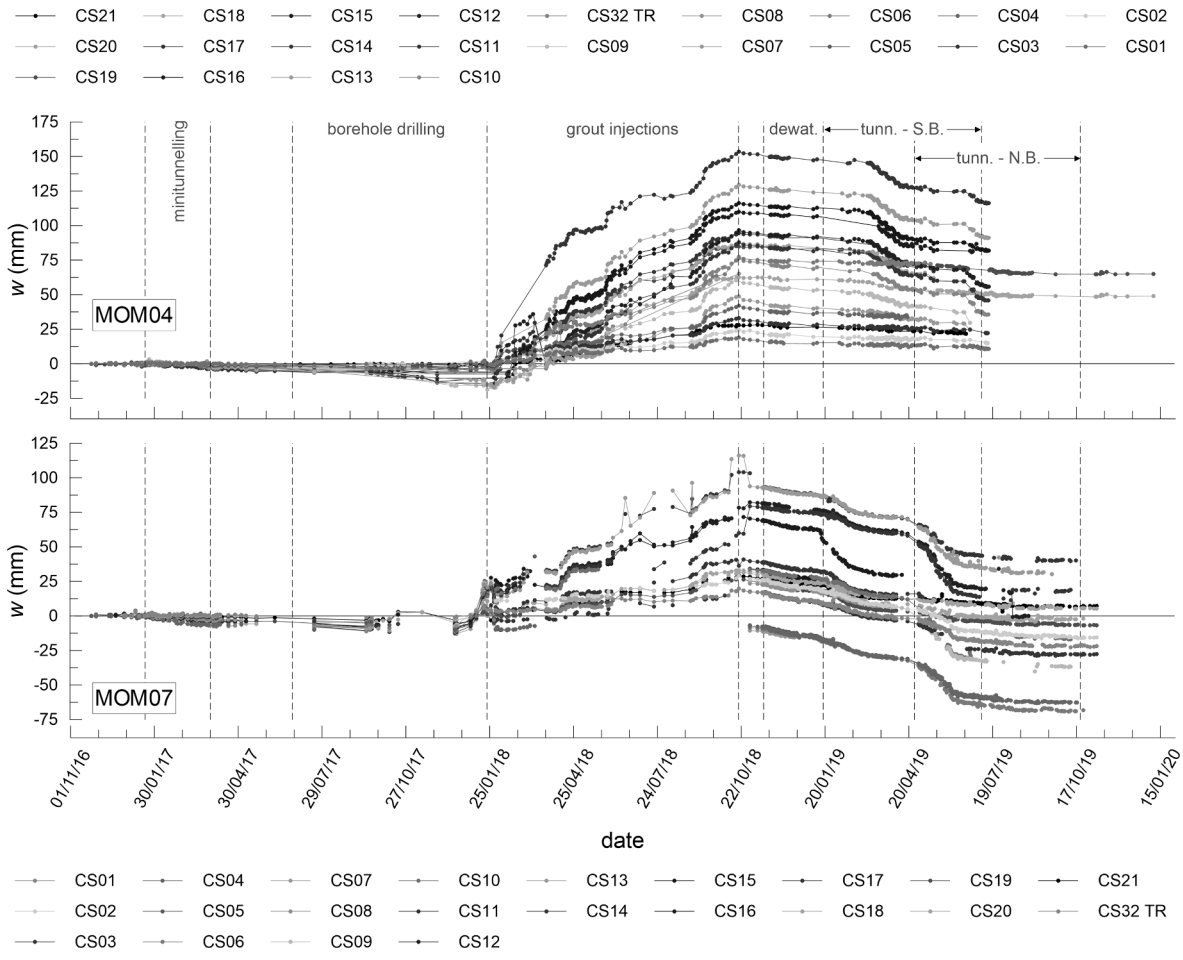


**Fig. 4.** Time histories of the vertical displacements measured at sections MOM04 and MOM07.

### 3.1. Slurry shield mini tunnelling

The settlements measured at the monitoring alignments were best fitted using a Gaussian distribution curve to evaluate the nominal volume loss induced by mini tunnelling. Prior to best fitting, the reference undeformed ground surface was determined for each instrumented section by averaging the displacement readings taken at distances of at least 30 m from the excavation face.

Fig. 5a shows the settlement profiles observed at the *green field* monitoring section (MOM-05–06-07), while Fig. 5b depicts the settlements measured at the instrument alignments in the presence of the barrier (MOM-02–03-04): from here on, zero abscissa refers to the axis of the southbound mini-tunnel.

Although the small settlements induced by mini tunnelling, the volume loss computed at ground surface was not negligible due to the tunnels small diameter, being equal to $V_L = 0.67–1.43$ % in *green field* conditions and to $V_L = 0.44–0.70$ % in the presence of the protective barrier. The barrier then reduced the volume loss of 34 to 51 %, though no appreciable change in the shape of the settlement trough was observed close to the barrier. In fact, due to the large cover to diameter ratio ($C/D = 7.8$ for the mini tunnels), the magnitude of the vertical displacements induced by mini tunnelling beyond the location of the barrier is comparable to the data scatter.

### 3.2. Soil improvement

The effects of radial borehole drilling were assessed for each settlement marker assuming the reference zero as the average displacement over the period from the end of mini-tunnels excavation to the start of the field injection test (Mar. 4 – Aug. 6, 2017). Similarly, the displacements caused by the radial grout injections were measured relative to the average value computed during the time interval ranging from the end of borehole drilling and the start of the injections (Oct. 9 – Dec. 20, 2017).

Fig. 6 plots the displacement profiles induced at ground surface by the radial borehole drilling, both in the absence and the presence of the barrier, respectively.

The Gaussian curve interpolating the displacement profiles induced by borehole drilling is seen to be less accurate, probably because of the irregular sequence adopted for drilling operations. The maximum settlement resulting from the installation of the *tubes à manchettes* is equal to −8.4 mm and −20.5 mm in *green field* conditions (sections MOM-07 and MOM-06) and to −4.6 mm and −13.1 mm in the presence of the barrier (sections MOM-02 and MOM-04). This time, the settlement trough becomes noticeably asymmetrical at the monitoring sections crossing the line of piles (sections MOM02 to MOM04), unlike what was observed during the mini tunnelling phase. Asymmetry of the settlement trough was probably appreciated at this stage due to the higher volume loss occurred during radial borehole drilling, equal to 1.49–6.31 % in *green field* conditions and to 0.69–3.19 % in the presence of the barrier.

Fig. 7 depicts the heave profiles caused by the grout injection phase for soil improvement. Despite the injections being conducted at pressure of about 10 MPa, a substantial heave was observed at ground surface with maximum values of about 115 mm in *green field* conditions. In the presence of the barrier, the heave was even higher and equal to about 165 mm. Moreover, the barrier was not capable to produce a significant reduction in the uplift of the ground behind its position, in the portion of the soil facing the *Aurelian Walls*. Indeed, the low efficiency of the barrier in reducing soil uplift during grout injections may be attributed to the short portion of the barrier embedded in the firm soil (i.e. outside the tunnel-induced displacement field). It has been shown that the barrier should be extended at least half a diameter below the tunnel invert to achieve a significant efficiency of the intervention. Shorter lengths can result in a large reduction in the efficiency (e.g.: Rampello et al., 2019). Fig. 2 shows that the barrier is long enough in the case of the mini and main tunnels. Conversely, in the case of the grout injections, where the equivalent diameter of the treated area is equal to about 14 m, the embedment length of the barrier is too short, reducing the efficiency of the intervention.

Except for the MOM-04 section, the Gaussian curve poorly approximates the displacement profile caused by the injections. This lack of accuracy can be attributed to the variability in the volume of grout injected by each valve and the irregular sequence of the injection process. Specifically, grout injection was repeated until a fixed threshold injection pressure was reached. The volume injected through a single valve ranged from 25 to 50 L until the threshold pressure was achieved. Consequently, the variability in the injected volumes per section may be thought as responsible for the significant scattering observed in the heave profiles.

### 3.3. Conventional tunnel excavation

#### 3.3.1. Dewatering and southbound tunnel excavation

The excavation of the southbound main tunnel was stopped 5 days after its beginning (Nov. 15, 2018) due to the basal heave of the treated soil with water entering the tunnel. Sixteen pumping wells (see Fig. 1) were activated to reduce the pore water pressure acting at the base of tunnel, the excavation being resumed about two months later (Jan. 18, 2019).

Pumping from the relief wells lowered the piezometric head by approximately 9.5 m in the layer of sandy gravel (SG), allowing safe tunnel excavation, although dewatering increased the effective stress in

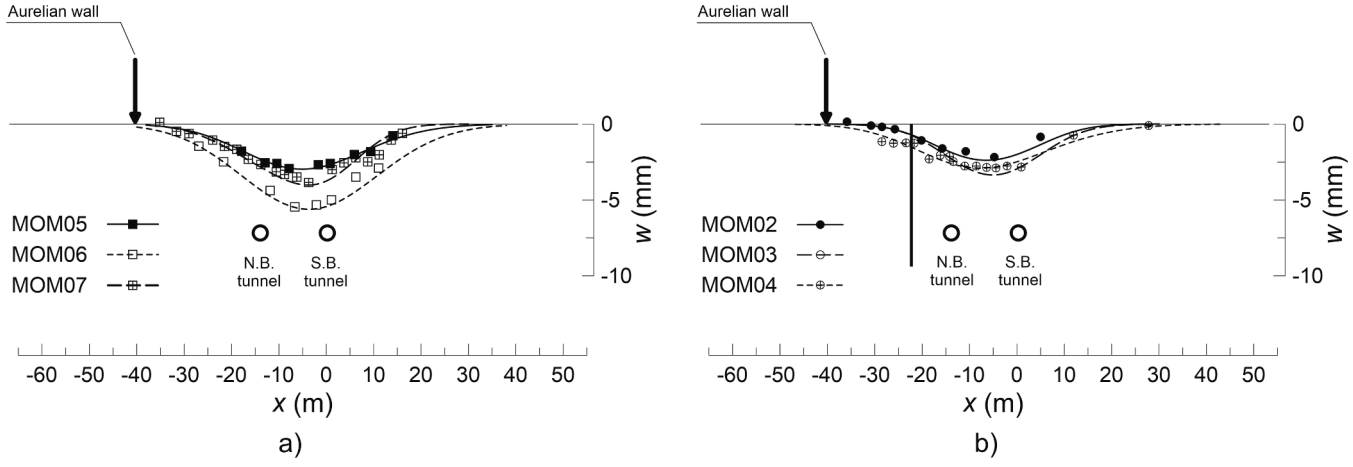


**Fig. 5.** Settlement profiles induced by mini-tunnelling: (a) *green field* monitoring sections (MOM-05–06-07); (b) in the presence of the barrier (MOM-02–03-04).

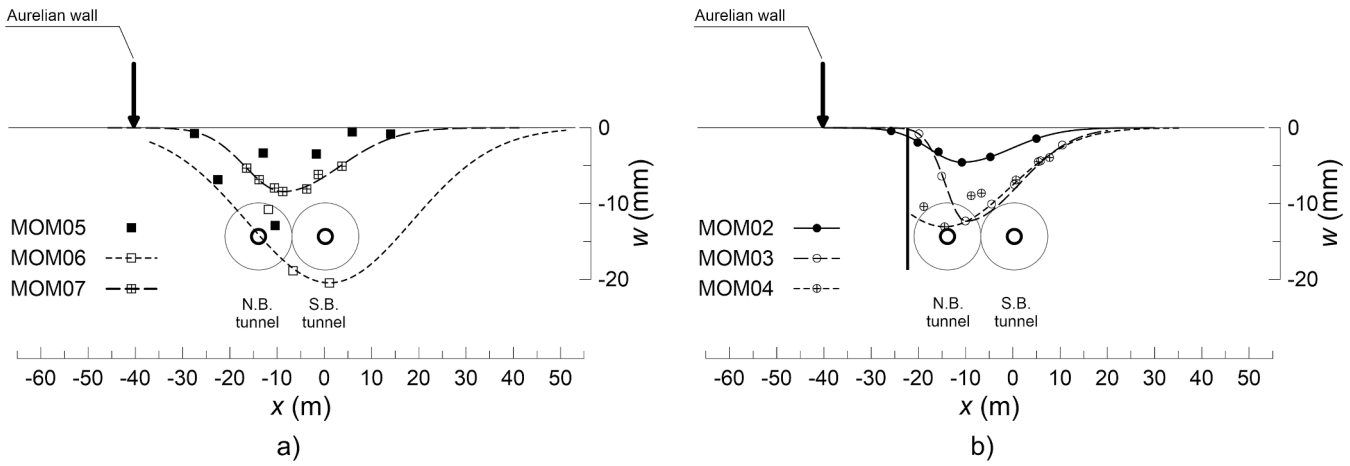


**Fig. 6.** Settlement profiles induced by radial borehole drilling: (a) *green field* monitoring sections (MOM-05–06-07); (b) in the presence of the barrier (MOM-02–03-04).

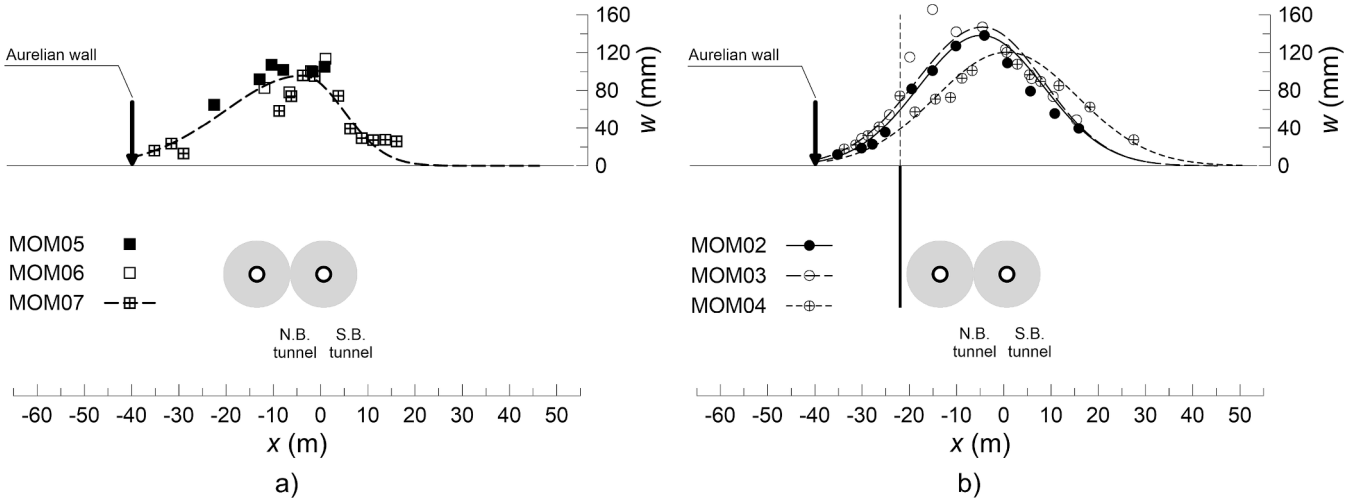


**Fig. 7.** Settlement profiles induced by low-pressure grout injections: (a) *green field* monitoring sections (MOM-05–06-07); (b) in the presence of the barrier (MOM-02–03-04).

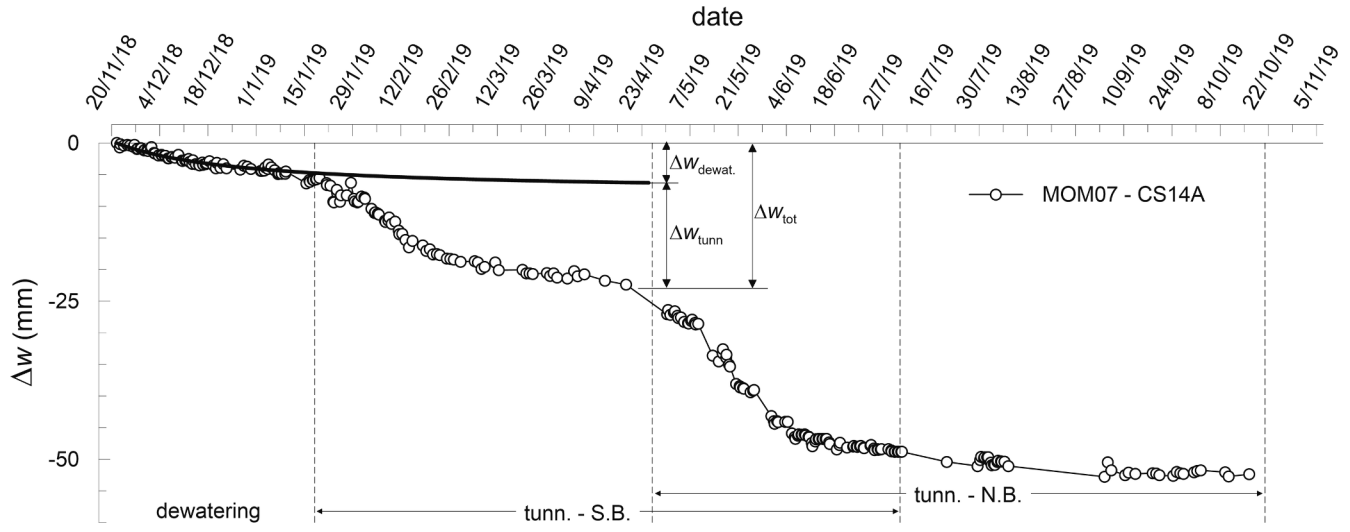


**Fig. 8.** Time-history of the relative settlements measured at the displacement marker CS14 of section MOM07 during dewatering and conventional tunnelling activities.

the clayey silt layer, resulting in additional surface settlement.

To evaluate the impact of dewatering, the time required for the consolidation of the alluvial fine-grained silty layer (CS-SS) was evaluated using the Terzaghi's theory of one-dimensional consolidation, assuming a consolidation coefficient $C_v = 10^{-4}$ m$^2$/s and a drainage path equal to 12.3 m, this corresponding to the thickness of the silty layer below the water table, found at depth $z = 14$ m. It was estimated that the consolidation process would have been completed in about 18 days, concluding that the settlements induced by dewatering were mostly developed prior to the restart of tunnel excavation.

Fig. 8 shows the procedure adopted to isolate the effect of dewatering on settlement marker CS14 of the MOM-07 alignment; the same procedure was used for each settlement marker. Settlements are plotted relative to the beginning of dewatering from the relief wells (Nov. 11, 2018). The first part of the curve exhibits a gradual increase in settlements, which can be attributed to the consolidation process caused by the dewatering, while the second part shows a steeper increase associated with the excavation of southbound tunnel first and northbound tunnel after. The initial portion of the curve was best-fitted using a hyperbolic function with the origin corresponding to the start of the pumping activities, allowing the final settlement induced by dewatering to be estimated. The settlements caused by tunnel excavation only were then determined from the difference between the measured settlements and those attributed to dewatering.

Fig. 9 shows the profile of settlements induced by the consolidation process activated by the dewatering activities. All the monitoring arrays exhibit a similar behaviour with a maximum settlement of about 7 mm above the two tunnels. The barrier, consisting of adjacent piles partially embedded in the layer of sandy gravel, was obviously not able to act as an impermeable screen to mitigate the effect induced by the pumping activities. It is worth noting that the consolidation settlement computed by the 1D consolidation theory assuming uniform drawdown provides a settlement equal to about 3 cm if the compression parameters of the silty layer (CS-SS) are considered, against an observed value slightly lower than 1 cm. This suggests that dewatering mainly affects the portion of the silty layer treated with grout injection and located between the two lines of pumping wells, that is characterised by a much lower compressibility.

Fig. 10 depicts the settlement trough caused by the excavation of the southbound tunnel. In the following, zero abscissa refers to the axis of the southbound tunnel. For the *green field* sections, the maximum settlements occurred approximately above the tunnel axis, ranging from −27.5 mm (MOM-07) to −21 mm (MOM-05). MOM-07 and MOM-06 sections exhibited similar responses in terms of maximum settlement ($w_{max}$ = -27 mm) and volume loss ($V_L$ = 2.42 %). However, the settlement trough observed at section MOM-07 was slightly wider on the negative side of the *x*-axis, possibly due to the local collapse mechanism triggered at the beginning of the excavation. MOM-05 section, located

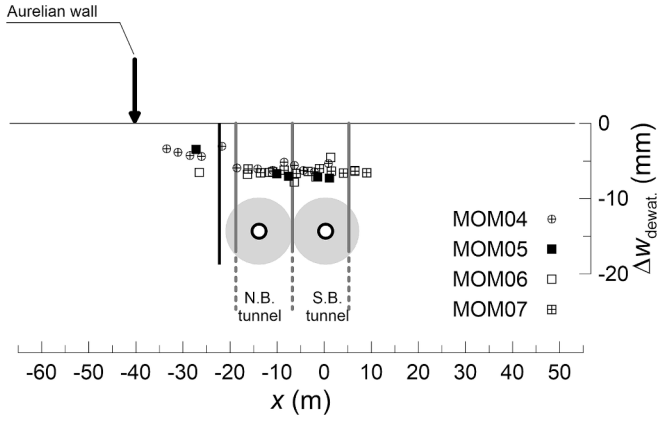


**Fig. 9.** Observed relative settlements induced by the dewatering activities.

only 1.5 m away from the edge of the barrier, experienced slightly lower settlements, $w_{max}$ = -21 mm, and volume loss, $V_L$ = 2.01 %, compared to the other *green field* sections. Surface settlements evaluated for the *green field* sections at the location of the *Aurelian Walls* ranged from −16.7 mm (MOM-07) to −11.2 mm (MOM-05).

Lower settlements were observed along the sections interacting with the protective barrier (Fig. 10b): the maximum settlements above the axis of the southbound tunnel was equal to −16 mm for alignment MOM-02 and −19 mm for MOM-04, while for section MOM-03 it was $w_{max}$ = -26.5 mm. However, despite the larger maximum settlement, the volume loss measured at section MOM-03, $V_L$ = 1.28 %, was in the range of the values obtained for sections MOM-04 and MOM-02, $V_L$ = 1.37 % and 0.84 %, respectively, with a volume loss reduction of 32 % to 65 % compared to the *green field* sections. At the location of the *Aurelian Walls*, the surface settlements were negligible this time, while next to the embedded barrier the measured settlements decreased by approximately 53 % to 87 %, ($w_{max}$ = -2.2 and −5.3 mm for MOM02 and MOM04), demonstrating the effectiveness of the protective barrier in mitigating the effects of tunnelling.

### 3.3.2. Northbound main tunnel excavation

Fig. 11 depicts the measured settlement troughs associated with the excavation of both tunnels. The *green field* sections (Fig. 11a) exhibit higher settlements, reaching a maximum value $w_{max}$ = -76 mm at about the mid-plane between the tunnels in the MOM-06 section. Due to the availability of only 4 settlement markers, data interpolation with the Gaussian curve was not possible for section MOM-06. An asymmetrical settlement trough is observed for section MOM-07, attributed to the larger cross-section of the northbound tunnel (see Fig. 1). Consequently, separate best-fitting of the measured settlements were performed to the right (+) and the left (−) of the maximum value with a trough width factor $i^{(-)}$ = 22.7 m significantly higher than $i^{(+)}$ = 13.4 m. Surface settlements at the location of the *Aurelian Walls* were also higher in section MOM07, about −20 mm, compared to section MOM05, for which settlements around −12 mm were measured.

For the sections interacting with the protective barrier (Fig. 11b), lower settlements were observed both above the tunnels and near the *Aurelian Walls*. Maximum settlements above the tunnels ranged from −26 mm to −44 mm, while surface settlements at the location of the *Aurelian Walls* did not exceed −5 mm. A settlement reduction of 58 % was achieved at the wall façade, whereas settlements measured at the embedded barrier location were reduced by approximately 72 %, with the settlement measured at the same abscissa being −43 mm in *green field* conditions (sect. MOM-05, Fig. 11a) and −12 mm in the presence of the embedded barrier (MOM 04–03-02, Fig. 11b). The effectiveness of the protective barrier is also evident when considering the volume loss calculated in the absence and the presence of the barrier, $V_L$ = 2.60 % (sect. MOM-05) against $V_L$ = 0.96 %-1.31 %, with an average reduction of about 56 %.

To quantify the effectiveness of the passive barrier in reducing the tunnelling induced displacement field, the local efficiency at a given distance *x* from the barrier is defined as (Bilotta, 2008):

$$\eta_{loc}(x) = 1 - \frac{w_b(x)}{w_{ff}(x)} \tag{1}$$

where $w_b(x)$ and $w_{ff}(x)$ are the settlements computed in the presence of the barrier and in free-field conditions, respectively. Similarly, an integral efficiency may be defined, that provides an overall index of the settlement reduction, considering the areas of the transverse settlement troughs computed with and without the barrier, behind its location:

$$\eta_{int} = 1 - \frac{\int_{x_b}^{x_m} w_b(x)\cdot dx}{\int_{x_b}^{x_m} w_{ff}(x)\cdot dx} \tag{2}$$

where $x_b$ and $x_m$ are the abscissa corresponding to the external side of

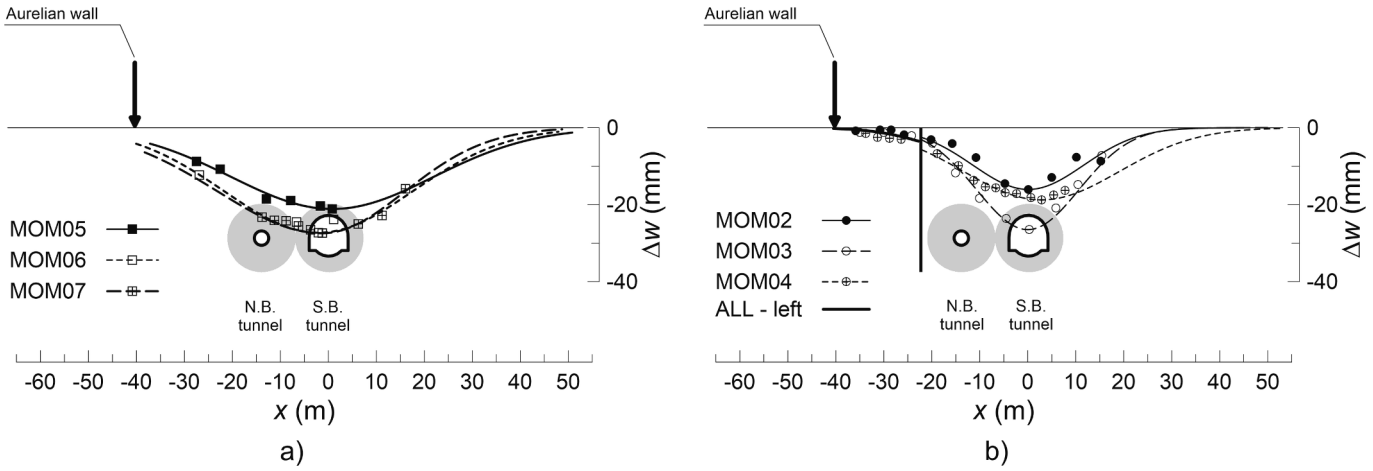


**Fig. 10.** Relative settlements profiles induced by the excavation of the southbound tunnel at: (a) the *green field* monitoring sections MOM-05–06-07; (b) in the presence of the barrier (sections MOM-02–03-04).

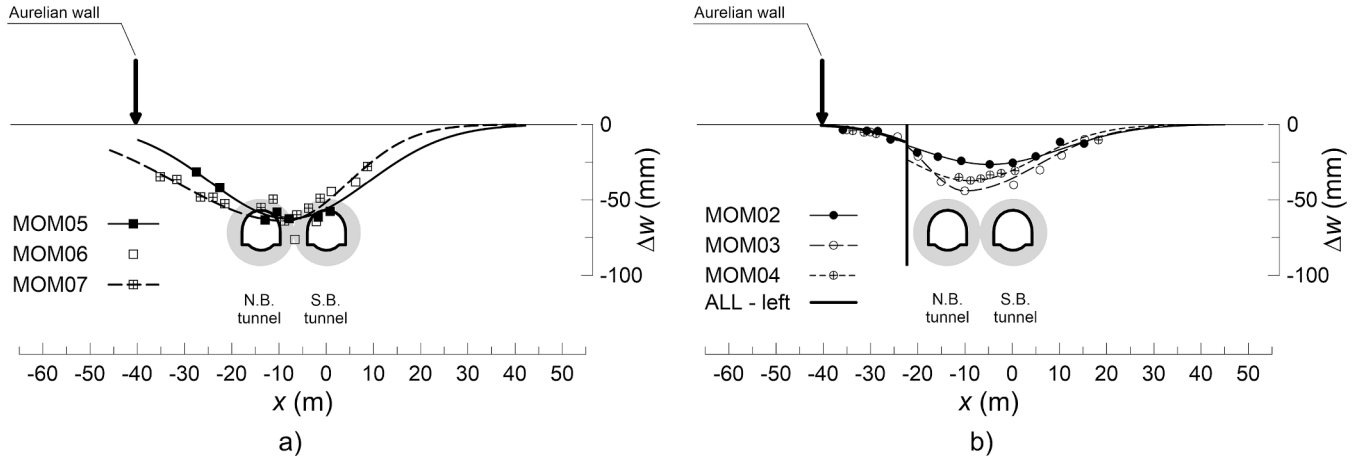


**Fig. 11.** Relative settlements profiles observed at the end of the excavation of the northbound at: (a) the *green field* monitoring sections MOM-05–06-07; (b) in the presence of the barrier (sections MOM-02–03-04).

the barrier and the distance for which $w_b(x) = w_{ff}(x)$.

Both the local and the integral efficiencies are equal to zero when no settlement reduction is obtained, while they approach the unity as the settlements in the presence of the barrier tend to zero (maximum efficiency). Table 3 reports the average values of the integral ($\eta_{int}$) and the local ($\eta_{loc}$) efficiencies, the latter computed just behind the barrier, as obtained from the field data. Both decrease with increasing $C/D$ ratio, as expected, with values higher than 50 %. However, the high efficiency observed for mini-tunnelling is somehow less reliable due to the small induced settlements, that are comparable to the data scatter.

## 4. SSI FE analyses

### 4.1. Numerical model

The analysis of the monitoring data highlighted the complexity of the interaction between the various stages of construction. To identify and isolate the deformation mechanisms associated with the different working activities and understand their interaction with the protective barrier, a FE back-analysis of the displacements observed at ground surface was performed under plane strain conditions (Plaxis 2D, Brinkgreve et al., 2014). In the analyses, the tunnels axis was assumed at a constant depth $z = 24$ m and the axis of the North-bound tunnel at 26.4 m from the Aurelian Walls, which is the lowest distance in the actual tunnel layout. Fig. 12 illustrates the numerical model adopted and the standard fixities applied to the boundaries.

The mechanical behaviour of the made ground (MG), the sandy gravel (SG) layer, and the overconsolidated stiff clay (OSC) was described using the *Hardening Soil model* (HS) (Schanz et al., 1999), while the behaviour of the alluvial deposits consisting of the clayey silt and the sandy silt (CS-SS), for which accurate laboratory test results were available (Rampello et al., 2019), was described using the *Hardening Soil model with small-strain stiffness*, *HSsmall* (Schanz et al., 1999; Benz et al., 2009). The calibration of the strength and stiffness parameters of the constitutive models from in situ and laboratory tests is discussed by Rampello et al. (2019) and Masini and Rampello (2021). For ease of reference, Table 4 provides a summary of the input parameters adopted in the analysis for the soil. Due to the high permeability ($k = 10^{-5}$ m/s) of the made ground (MG) and the sandy gravel (SG), and the medium permeability ($k = 0.25\text{-}1{\cdot}10^{-5}$ m/s) of the alluvial deposits (CS-SS), the FE analyses were performed in terms of effective stresses,

**Table 3**
Integral and local efficiency obtained from the monitoring data (average values).

| | $C/D$ | $\eta_{int}$ | $\eta_{loc}$ |
|---|---|---|---|
| mini tunnelling | 7.8 | 66 % | 50 % |
| conventional excavation | 2.6 | 88 % | 72 % |

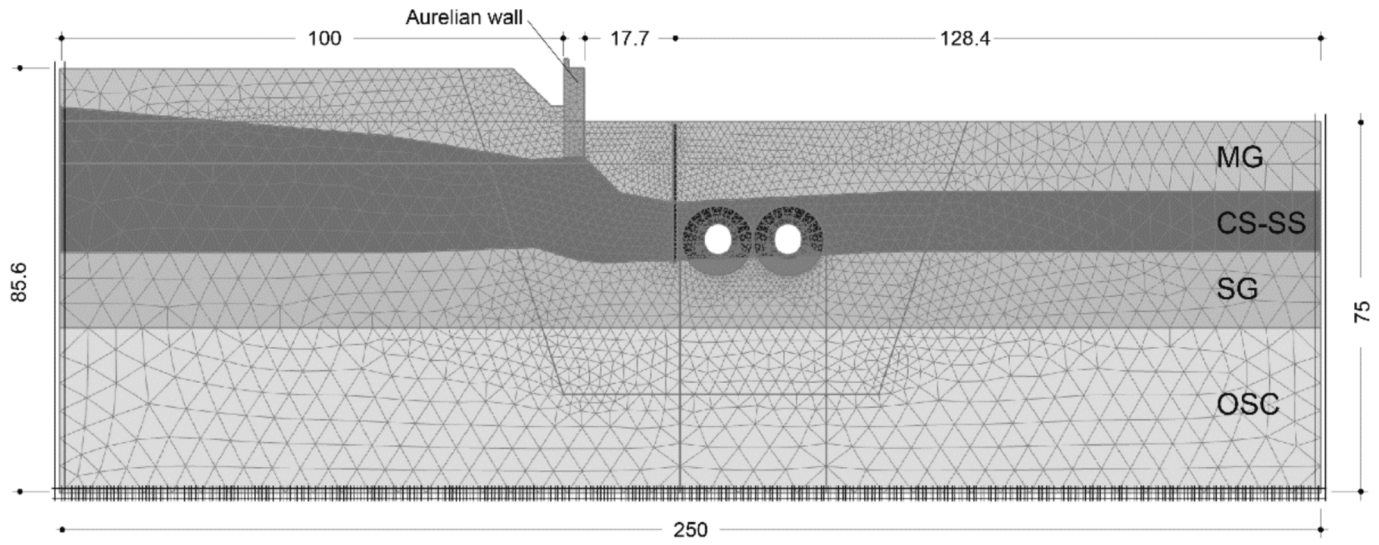


**Fig. 12.** 2D mesh adopted for the numerical analyses.

**Table 4**
Soil parameters from in situ and laboratory tests and input parameters for FE SSI analyses.

| soil | γ (kN/m$^3$) | c' (kPa) | φ' (°) | YSR (–) | $K_0^{nc}$ (–) | $E'^{ref}_{ur}$ (MPa) | m (–) | $E'_{ur}/E'_{50}$ (–) | $E'_{oed}/E'_{50}$ (–) | $G_0$ (MPa) | $\gamma_{0.7}$ (%) | k (m/s) |
|---|---|---|---|---|---|---|---|---|---|---|---|---|
| MG | 17 | 5 | 34 | 3.5 | 1 | 240 | 1 | 10 | 1 | – | – | $1{\cdot}10^{-5}$ |
| Sandy Silt (CS-SS) | 19.5 | 28 | 27 | 1.25 | 0.55 | 150 | 0.8 | 18.28 | 0.36 | 125 | 0.035 | $1{\cdot}10^{-6}$ |
| Sandy Gravel (SG) | 20 | 0.1 | 40 | 7.5 | 0.36 | 900 | 0.4 | 10 | 1 | – | – | $1{\cdot}10^{-5}$ |
| Stiff Clay (OSC) | 20.9 | 41.3 | 25.7 | 2.5 | 0.57 | 450 | 0.9 | 20 | 1 | – | – | $1{\cdot}10^{-10}$ |
| improved Sandy Silt | 19.5 | 28 | 27 | 1.25 | 0.55 | 180 | 0.8 | 9.85 | 3.54 | 125 | 0.035 | $2{\cdot}10^{-7}$ |
| improved Sandy Gravel | 20 | 20 | 40 | 7.5 | 0.36 | 1080 | 0.4 | 10 | 1 | – | – | $2{\cdot}10^{-6}$ |

assuming drained conditions. Undrained behaviour was instead assumed for the deep layer of overconsolidated stiff clay (OSC).

The *Aurelian Walls*, the lining of the running tunnels, and the barrier were modelled using solid elements, while the lining of the mini-tunnels and the temporary lining of the running tunnels were modelled using plate elements. Tables 5 and 6 summarise the properties of the structural elements used in the analyses. The *Aurelian Walls* were assumed to behave as a linear elastic-perfectly plastic material using the Mohr-Coulomb failure criterion with the same parameters adopted in the Metro C project. For the 2D modelling of the line of piles, a continuous equivalent diaphragm wall was used with reduced stiffness and weight to account for pile spacing (Rampello et al., 2019). Cohesionless interface elements were adopted at the soil-structure interfaces, reducing the angle of shearing resistance φ′ of the adjacent soil by a coefficient $R_{int} = 0.7$. To account for the discontinuous nature of the piled wall and the fact that shear stresses develop in the soil at the pile-soil interface for a cast-in-situ bored pile, a fully rough contact ($R_{int} = 1$) was assumed at the soil-barrier interface.

The calculation steps listed in Table 7 replicate the main construction stages discussed in the previous sections.

To compare the results of the numerical analyses with the free-field monitoring data, the simulation was repeated with the line of piles deactivated. Conversely, in the analyses with the barrier, the line of piles was assumed to be "wished-in-place" as the effects induced by tunnelling outweigh those induced by the installation of a line of piles (Rampello et al., 2019). The barrier was activated soon after the initialization of the effective stress state, before simulating the construction stages.

**Table 6**
Input parameters of plate elements for FE SSI analyses.

| element | modell | w (kN/m/m) | EA (MN/m) | EI (MNm$^2$/m) | thickness (m) | ν (–) |
|---|---|---|---|---|---|---|
| temporary lining | linear elastic | 4.6 | 6500 | 22.6 | 0.2 | 0.15 |
| mini-tunnel lining | linear elastic | 5 | 7500 | 56.3 | 0.2 | 0.15 |

### 4.2. Mini-tunnel excavation and soil improvements

The plane strain excavation of the mini-tunnels was simulated using a displacement-based approach, where a global contraction parameter $c_{ref}$ is applied to the tunnel lining as a percentage ΔA of the initial cross-sectional area $A_0$ of the tunnel, $C_{ref} = \frac{\Delta V}{V_0} \cdot 100$ ($c_{ref}$-method, Vermeer

**Table 5**
Input parameters of masonry and concrete elements for FE SSI analyses.

| element | model | γ (kN/m$^3$) | c' (kPa) | φ (°) | σ'$_t$ (kPa) | $K_0$ (–) | E (MPa) |
|---|---|---|---|---|---|---|---|
| Aurelian Walls | mohr–coulomb | 22 | 240 | 13 | 60 | 0.78 | 300 |
| barrier | linear elastic | 28.25 | – | – | – | 1 | 32,837 |
| final lining | linear elastic | 18.8 | – | – | – | 1 | 27 |

**Table 7**
Simulation stages.

| stage | description |
|---|---|
| 0 | initialization of the effective stress state with the observed downward seepage |
| 1 | activation of the *Aurelian Walls* and the backfill |
| 2 | relief excavation at the back of the *Aurelian Walls* |
| 3 | activation of the protective barrier |
| 4 | excavation of the southbound mini-tunnel |
| 5 | excavation of the northbound mini-tunnel |
| 6 | simulation of the radial borehole drilling |
| 7 | simulation of the radial injections |
| 8 | pumping from the relief wells |
| 9 | excavation of the southbound main tunnel |
| 10 | excavation of the northbound main tunnel |

and Brinkgreve, 1993). The procedure involves deactivating the soil elements within the tunnel first, then activating the lining elements, and finally applying the global contraction ($c_{ref}$).

Since the barrier did not significantly affect the shape of the surface settlement trough induced by mini-tunnelling (Fig. 5), parameter $c_{ref}$ was evaluated by trial and error to match the settlement profiles observed in the monitoring sections with the barrier, characterised by less data scatter. Specifically, a contraction factor $c_{ref} = 0.91$ % and 0.85 % was adopted for the southbound and the northbound mini-tunnel, respectively.

Soil improvement was simulated in two stages: (*i*) a reduction of the effective stress induced by borehole radial drilling in the surrounding soil; and (*ii*) an increase of the effective stress due to soil compaction produced by grout injections, with an increase in the strength and stiffness properties of the treated soil. To simulate these effects, a non-uniform volumetric deformation was applied to the treated soil, assuming a circular treated area around each mini-tunnel, with an equivalent diameter equal to twice the length of the *tubes à manchettes* (14.2 m); in addition, the stiffness and strength parameters of the treated soil were increased as reported in Table 4. Each area was divided into 11 sectors, starting from the springline of the mini-tunnels, with decreasing volumetric strains assigned to each sector moving from the crown to the springline. The values of the volume contraction (radial drilling) and expansion (grout injection phase) were obtained by trial and error to match the observed displacement profiles of the monitoring sections.

Specifically, the drilling phase was simulated by applying a volume contraction of 0.620 % at the crown of the tunnels, which was symmetrically reduced to 0.003 % at the springline. Conversely, the grout injection phase was simulated by applying a volume expansion of 17.3 % at the crown of the tunnels, which was symmetrically reduced to 0.48 % at the springline.

The contour lines of the horizontal effective stress $\sigma'_x$ computed at the end of soil improvement are plotted in Fig. 13a, while Fig. 13b shows the same contours of $\sigma'_x$ when soil improvement is simulated simply by changing the mechanical properties of the treated soil. Although the largest increases in $\sigma'_x$ are induced at the crown of the treated area, a significant change in the effective stress can also be observed in the volume of soil affected by the subsequent excavation of the main tunnel and at the location of the barrier.

Fig. 14 shows the contour lines of vertical displacements computed in the absence and the presence of the barrier at the end of the grout injection phase. The comparison between the monitoring data and the profiles of the vertical displacement computed at ground surface is also plotted in the figure. The FE model shows a fair agreement with the monitoring data in the *green field* section (Fig. 14a), while larger reductions of displacements are computed close to the *Aurelian Walls* in the sections affected by the barrier (Fig. 14b) compared to the observed behaviour. This could be partly due to the discontinuity of the line of piles which allows the propagation of the displacement field, while in the 2D FE model the barrier is simulated as an equivalent continuous diaphragm wall.

### 4.3. Dewatering and conventional main tunnels excavation

The pore water pressure changes resulting from the activation of the relief wells were simulated by assigning a hydraulic head $h = 7$ m a.s.l. to the boundary of their slotted section, which is embedded in the layer of sandy gravel (SG) for about 15 m. Fig. 15 shows the contour lines of the hydraulic head computed at the end of the steady-state seepage calculation. The calculated hydraulic head decreases mainly around the tunnels, but also slightly below the *Aurelian Walls*. Consequently, the computed contours lines of the incremental settlements induced by the dewatering process, plotted in Fig. 16, show values of $\Delta w_{dewat} = 3$–4 mm near the *Aurelian Walls*, while $\Delta w_{dewat}$ is equal to about 7 mm around the relief wells. Fig. 16 also shows the comparison between the observed and computed settlement troughs at ground surface: the dotted line refers to the FE analysis in which the soil treatment was simulated as *wished-in-place* (W.I.P.), by simply increasing the stiffness and strength properties of the treated area (Table 4), while the solid line refers to the analysis in which the borehole drilling and grout injections were simulated by volume contraction and subsequent expansion of the treated area, respectively. In the case of the simple activation of the treated soil, the computed settlement trough does not satisfactorily reproduce the observed subsidence: higher settlements develop in the soil under the *Aurelian Walls*, as a consequence of the normal consolidation state attained below the wall after the backfilling occurred in medieval age. Conversely, a close match in the shape of the settlement profile is

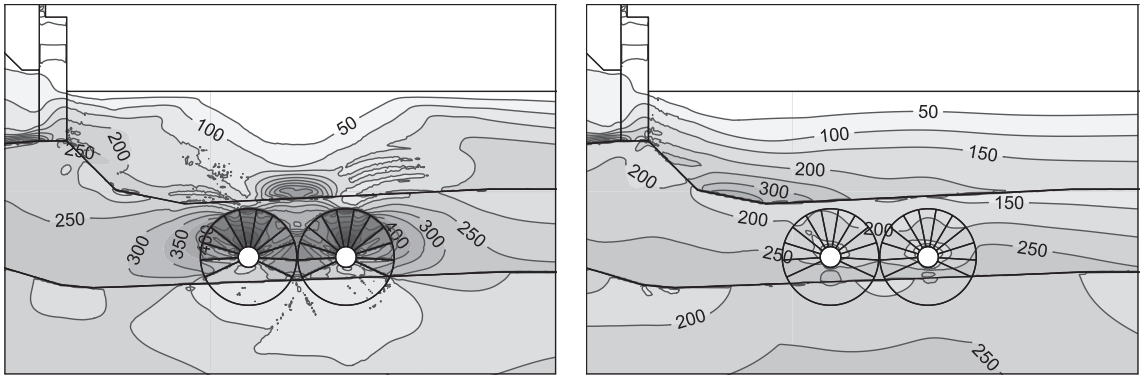


**Fig. 13.** Contour lines of the horizontal effective stress computed at the end of soil improvement: (a) volume contraction/expansion applied; (b) ideal installation and injection (values in kpa).

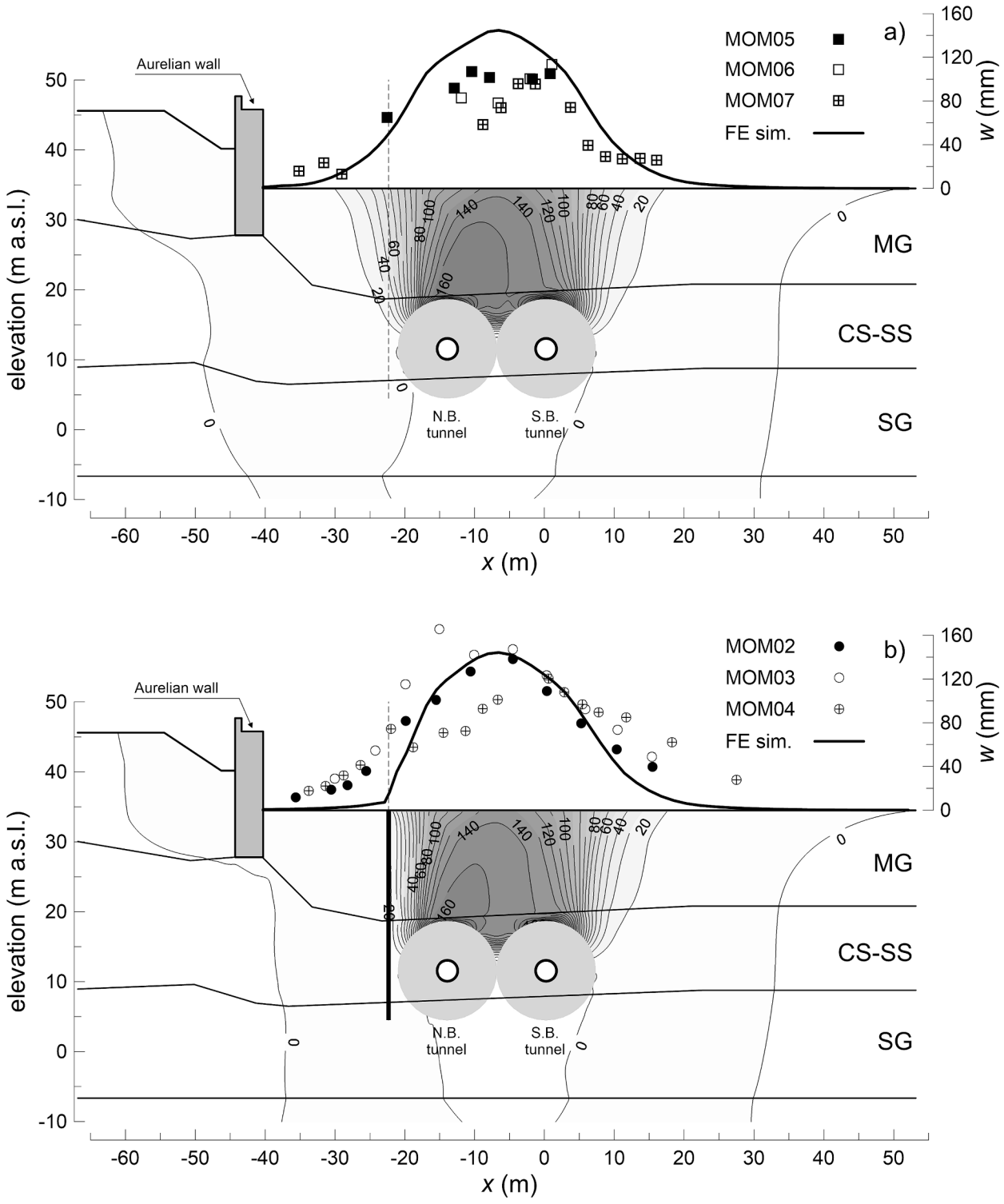


**Fig. 14.** FE analyses, contour lines of vertical displacements computed (a) in the absence and (b) in the presence of the barrier at the end of the injection phase (values in mm).

obtained when modelling the installation effects associated to borehole drilling and grout injection through calibrated volume changes of the treated area. This better agreement can be attributed to the increase in the horizontal effective stress induced by the grout injections in the soil at the tunnel spring line and towards the *Aurelian Walls* (Fig. 13), where the confining effective stress increases and the settlement decreases.

Plane strain simulation of conventional excavation of the two running tunnels was carried out using the force-based relaxation method (e.g. Schikora and Fink, 1982; Potts and Zdravković, 2001; Mroueh and Shahrour, 2008 among others). The soil elements within the tunnel were first removed and the nodal forces acting at the tunnel boundary were reduced by a stress release ratio λ; the lining elements were then activated and the residual (1-λ) nodal forces were transferred to the lining. A stress release ratio $\lambda = 0.8$ was evaluated assuming a distance of 1 m of the temporary lining from the tunnel face and using the longitudinal displacement profile (*LDP*) by Vlachopoulos and Diederichs (2009)

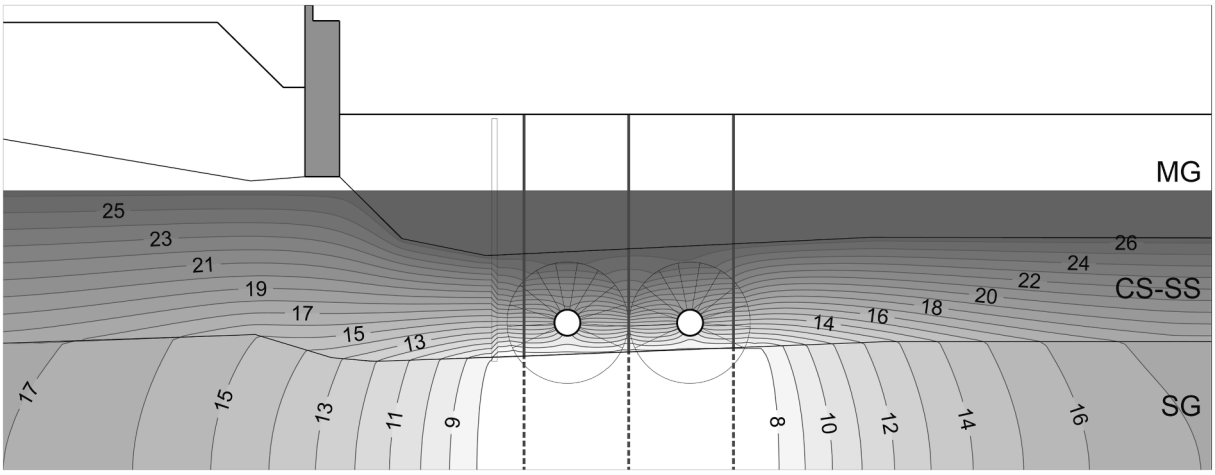


**Fig. 15.** Dewatering. contour lines of the hydraulic head (values in meters above the sea level).

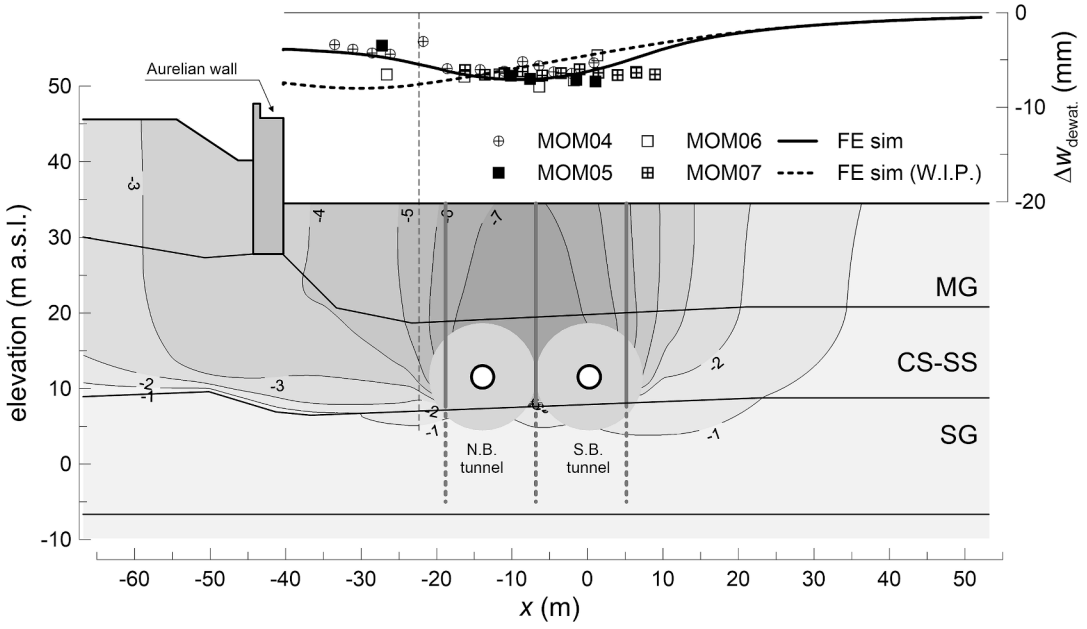


**Fig. 16.** FE analyses, contour lines of the incremental settlements ($\Delta w_{dewat.}$) computed at the end of the dewatering phase (values in mm).

together with the ground reaction curve (*GRC*) by Ribacchi and Riccioni (1977), the latter with the mechanical parameters of the CS-SS layer (Table 4).

Fig. 17 compares the settlement profiles measured by precision levelling at the surface displacement markers with those calculated at the end of excavation of the southbound tunnel. The contours of the displacement field calculated with and without the barrier are also shown in the figure.

The computed settlement profiles are in a good agreement with both the settlement troughs observed in the absence and presence of the protective barrier (Fig. 17a and 17b). Specifically, for the *green field* sections (Fig. 17a), the calculated maximum settlement and volume loss, $w_{max}$ = –23.7 mm and $V_L$ = 2.02 %, are within the measured range for $w_{max}$ = -21.1 mm to −27.4 mm, and $V_L$ = 2.01 % to 2.42 %. In the presence of the barrier, the FE analyses provided values of $w_{max}$ = 20 mm and $V_L$ = 2.02 % consistent with the measured ranges of $w_{max}$ = -16 mm to −26.5 mm and $V_L$ = 0.84 % to 1.37 %. Therefore, in the presence of the barrier there is a reduction in $w_{max}$ and $V_L$ of 15.6 % and 34.7 % respectively. Numerical simulations also show a good agreement with the monitoring data at the barrier location, with a calculated settlement reduction (about 70 %) within the measured range (53 %–87 %).

The comparison between the observed and computed settlement troughs at the end of excavation of both the tunnels is shown in Fig. 18a and 18b in the absence and the presence of the barrier, respectively.

For the *green field* sections (Fig. 18a), the computed settlement profile underestimates the observed response to the excavation of both the running tunnels, with a maximum settlement, $w_{max}$ = -43.2 mm, and a computed volume loss, $V_L$ = 1.49 %, about 32 % and 44 % lower than the measured values. However, a fair agreement is observed between the computed and measured settlements close to the *Aurelian Walls*, in that the settlements calculated at the locations of the wall and the barrier, $w$ = –23 mm and −38 mm, respectively, agree with the monitoring data. By contrast, in the presence of the barrier (Fig. 18b), the FE analyses were able to reproduce with a better accuracy the observed shape of the settlement trough. The maximum settlement $w_{max}$ = -30.7 mm was computed between the tunnels, closer to the first one, as also observed at section MOM-02. The computed volume loss $V_L$ = 1.31 % is in the range of the observed values, being 12 % lower than the one calculated in *green field* conditions. Between the *Aurelian Walls* and the barrier, the measured (−12 mm) and computed (−10 mm) settlements are in a very

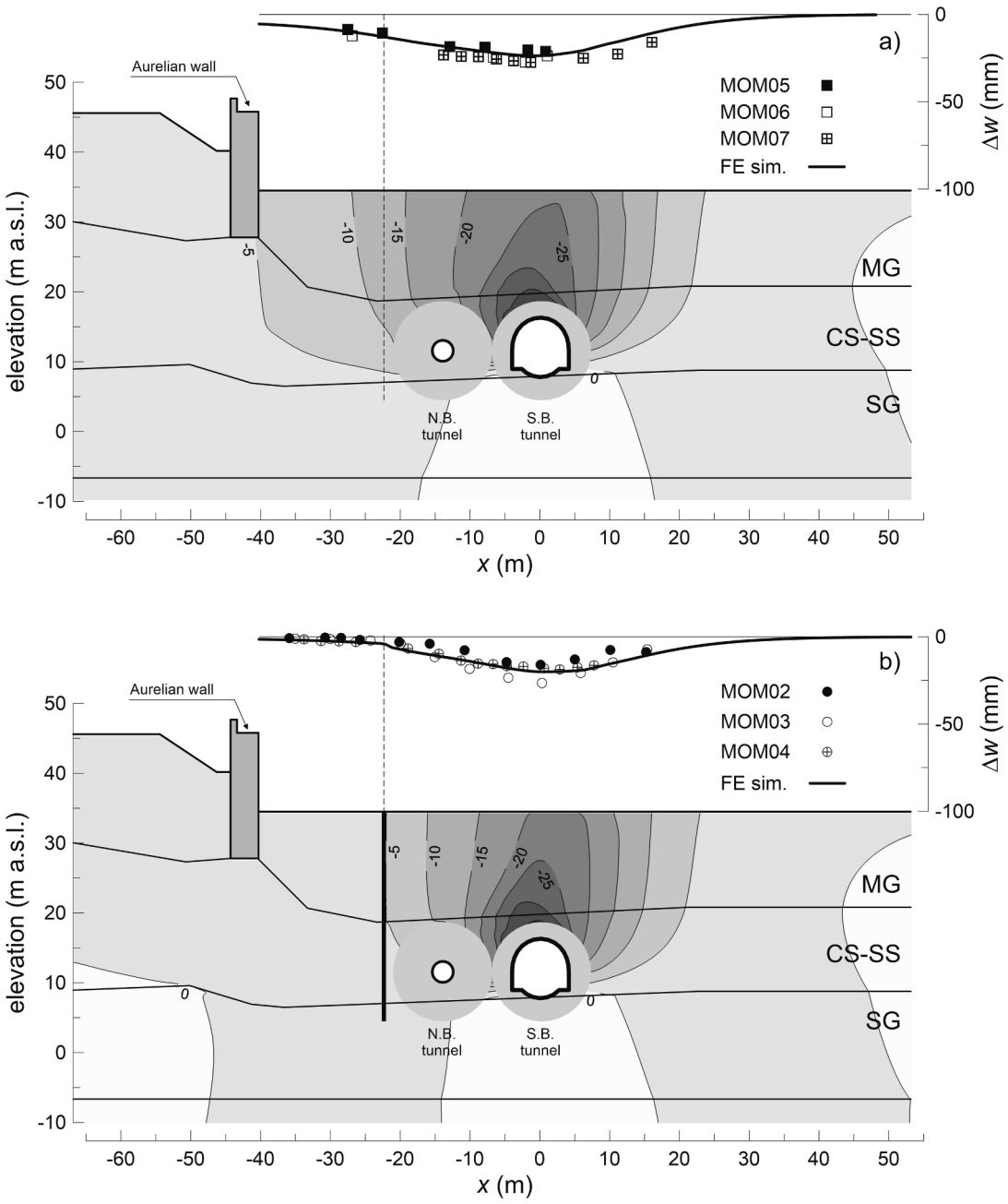


**Fig. 17.** FE analyses, contour lines of vertical displacements computed (a) in the absence and (b) in the presence of the barrier at the end of the southbound tunnel excavation (values in mm).

good agreement, with a computed settlement reduction at the location of the barrier equal to about 75 % compared to an observed value of 72 %.

## 5. The Aurelian Walls

The portion of the Aurelian Walls facing the tunnels was instrumented with electric tiltmeters installed at wall mid-height to measure the out-of-plane rotation and displacement markers installed at about 0.5 m above the ground surface for monitoring the vertical wall displacements (Fig. 1). The effects of conventional tunnelling alone are discussed below, as the TBM mini-tunnelling, borehole drillings and grout injections had negligible effects on the walls.

To assess the effects of conventional excavation of the southbound and northbound tunnels, the displacement measurements were referenced to the end of the injections (19/10/2018) and the baseline displacement profile of each section was assessed in the time interval between the end of the injections (19/10/2018) and the temporary cessation of southbound tunnel excavation (20/11/2018). Fig. 19 shows the isochrones of the wall settlements measured by precision levelling: the dotted lines refer to the excavation of the first tunnel (the southbound tunnel), while solid lines refer to the excavation of the second tunnel (the northbound tunnel). Negative abscissa in the figure refer to the displacement markers installed in the portion of the *Aurelian Walls* in front of the shaft (SL3-SL9). The first isochrone refers to the resumption of excavation of the southbound tunnel (18/01/2019) and shows that the dewatering operation caused a maximum wall subsidence of about 5 mm. At the end of the excavation of both tunnels, the maximum wall settlements were measured between the displacement markers SL9 and SL14, the former located in front of the corner of the TBM launching pit

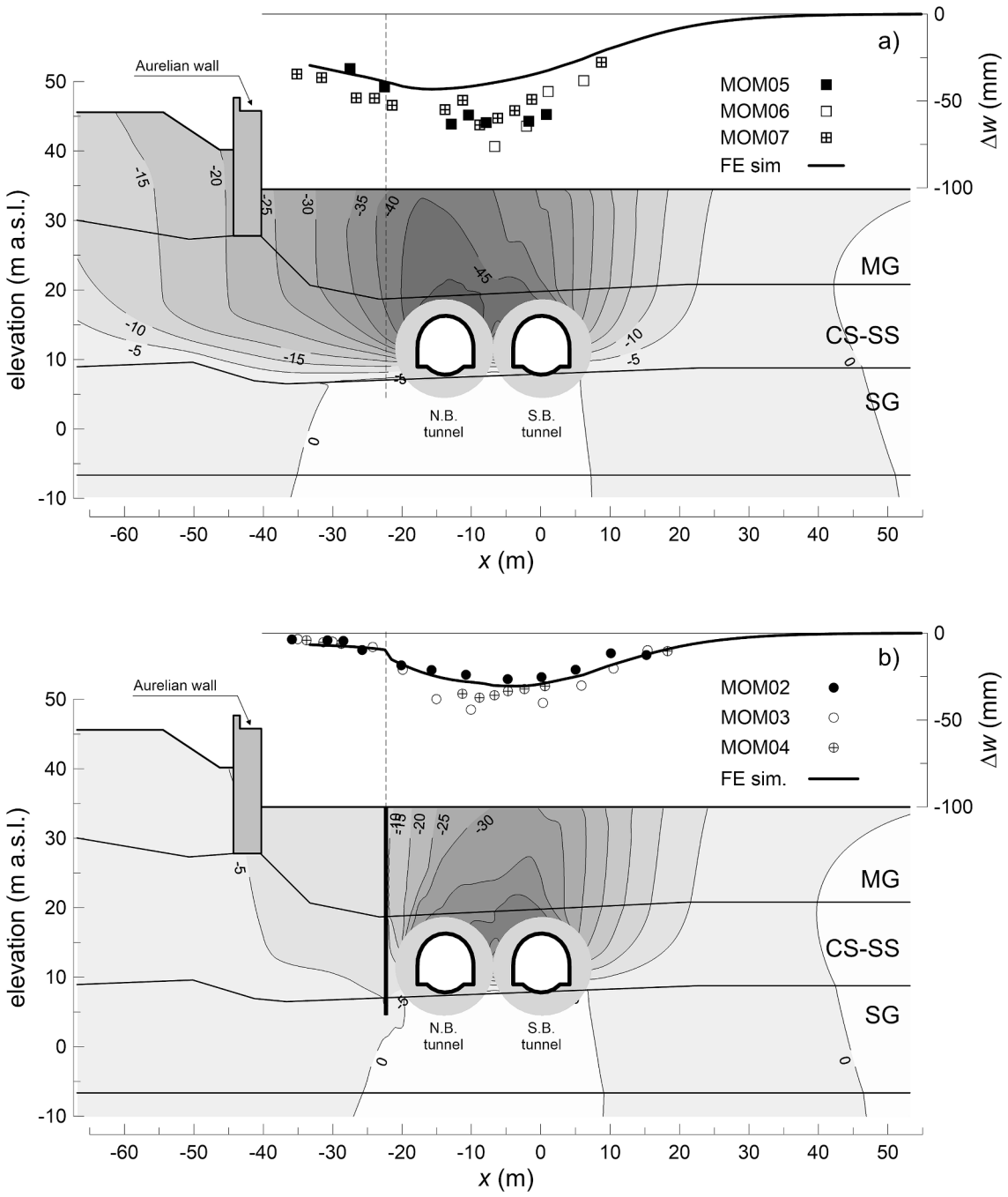


**Fig. 18.** FE analyses, contour lines of vertical displacements computed (a) in the absence and (b) in the presence of the barrier at the end of the northbound tunnel excavation (values in mm).

and the latter in front of the left edge of the barrier. In the portion of the wall located behind the barrier, the wall settlements decrease from 7 mm to about 2 mm from the displacement marker SL14 behind the left end of the barrier to the marker SL25 behind the right end of the barrier. With respect to the maximum wall settlement, which is approximately 12 mm (displacement marker SL12), a reduction of 43 % to about 84 % was then obtained, demonstrating the efficiency of this type of mitigation intervention. However, it should be noted that the observed reduction is also due to the slight increase in the distance between the northbound tunnel and the wall, as Porta Asinaria is approached. The maximum deflection ratios in sagging and hogging were $(\Delta_s/L_s)_{max} = 6.2{\cdot}10^{-5}$ and $(\Delta_h/L_h)_{max} = 2.7{\cdot}10^{-5}$, respectively, both substantially lower than the threshold values proposed by Burland and Wroth (1974): $(\Delta_s/L_s)_{lim} = 8{\cdot}10^{-4}$ and $(\Delta_h/L_h)_{lim} = 4{\cdot}10^{-4}$.

Tiltmeters CE 01D-02D-03D, installed in the portion of the wall facing the TBM launching pit, show nearly constant and negligible forward rotations, equal to about −0.03°, with similar values also observed for tiltmeters CE-04D and CE-06D, installed in portion of the wall near the shaft transverse diaphragm wall and the left end of the barrier, respectively (Fig. 1). By contrast, a maximum rotation of about −0.08° was measured on the CE-05D tiltmeter, installed close to the SL12 displacement marker, in the portion of the wall facing the MOM-06 *green field* array (Fig. 1).

Conversely, almost zero rotations were observed on the tiltmeters installed in the portion of the wall located behind the protective barrier (CE-07D, CE 01C–02C-03C in Fig. 1), showing once again the efficiency

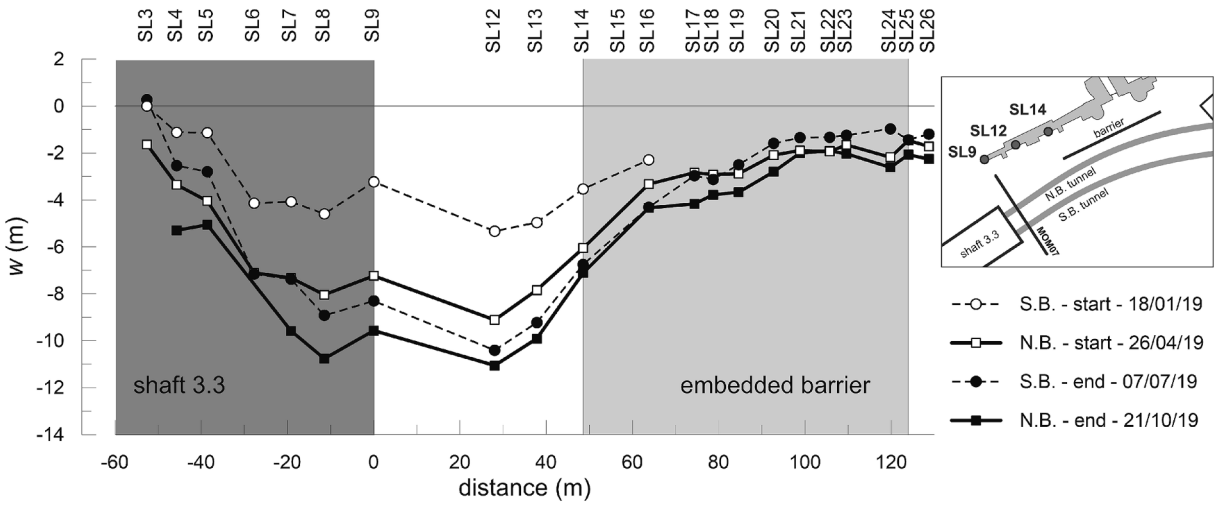


**Fig. 19.** Observed settlement profiles induced by tunnelling in the Aurelian Walls.

of the embedded barrier in reducing tunnelling effects on the ancient Aurelian Walls at *Porta Asinaria*.

Fig. 20 shows a scheme of the movements experienced by the wall cross section, obtained by assuming that the inner vertex A of the wall foundation does not move horizontally, which implies that the instantaneous centre of rotation lies on the plane passing through the base of the wall, and assuming a plane strain condition for both the sections shown in the figure. The measured reductions in settlement and rotation of the wall façade due to the presence of the barrier are 45 % and 75 %, respectively, while the corresponding computed values are equal to 79 % and 80 %. Therefore, while the computed settlement reduction appears somewhat overestimated, a closer evaluation of the wall rotation reduction was obtained, with a difference of only 5 % from the measured value.

## 6. Conclusions

A short stretch of conventional tunnelling of the line C of the Rome underground, located between the TBM launching pit and *San Giovanni* station, passes close to the ancient *Aurelian Walls* at *Porta Asinaria* with a potential damage induced to this monument of inestimable value. To limit the displacement field induced by the excavation activities, a three-step procedure was adopted during the construction phases: (i) excavation of two small-diameter tunnels with a mini slurry shield TBM; (ii) soil improvement by radial grouting from the mini-tunnels; and (iii) conventional excavation of the two main tunnels in the improved soil. To prevent any damage to the ancient city wall, a protective barrier of adjacent piles, partially embedded in the deep layer of sandy gravel, was installed prior to the excavation activities. The barrier is positioned about parallel to the city wall, between the northbound tunnel and the wall itself. The settlement markers, installed along 6 monitoring sections about transverse to the tunnels axis, permitted to evaluate the ground surface displacements and isolate the effects of the mini-tunnels excavation, ground improvement and conventional tunnelling. The monitoring data also enabled to assess the efficiency of the protective barrier in reducing the movements induced on the *Aurelian Walls* by the excavation stages.

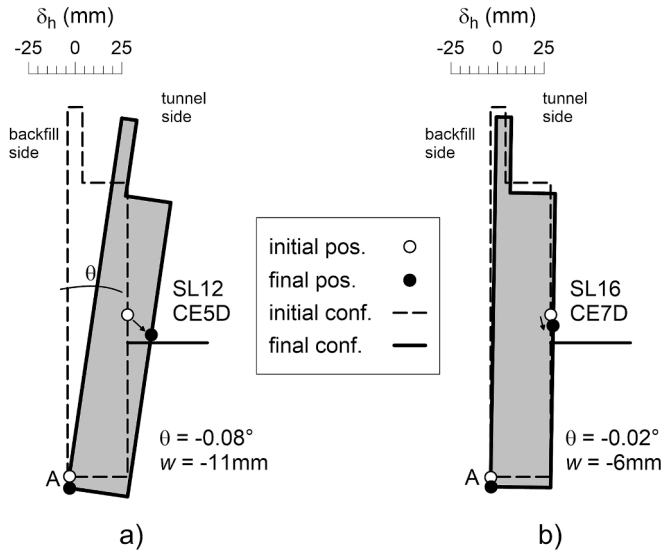


**Fig. 20.** Scheme of wall movements (a) in the absence (displacement marker SL12) and (b) the presence of the barrier (displacement marker SL16).

The main results of the monitoring data can be summarised as follows:

– after completion of the mini-tunnels, the volume loss computed from the surface settlement markers was relatively high ($V_L = 1.43$ %), although the maximum settlement was as small as 5 mm due to the high cover to tunnel diameter ratio ($C/D = 7.8$);

– radial borehole drilled from the mini-tunnel to install the *tubes à manchettes* produced maximum settlements about 4 times higher than those induced by the mini-tunnelling (~20 mm);

– at the location of the *Aurelian Walls*, the effects induced by both mini-TBM excavation and radial drilling were negligible, causing displacements smaller than 2 mm, with no clear appreciable mitigation effect of the barrier;

– the subsequent injection of grout, carried out at approximately 10 MPa, resulted in a significant heave of the ground surface, about 10 times higher than the settlements induced by borehole drilling (96 to 166 mm). At the location of the *Aurelian Walls*, the ground surface heave was of about 8 mm irrespective of the presence of the barrier, with no detrimental effect on the city wall.

Therefore, a careful monitoring of the ground surface settlements evidenced that some intermediate workings phases, such as grout injections, can produce non-negligible effects that, in principle, should be considered in the design. It has been shown that these effects can produce ground movements of the same order of magnitude as those induced by tunnels excavation.

With regard to the efficiency of the pre-installed barrier, consisting of a line of adjacent piles, the monitoring of ground movements demonstrated that:

– it proved to be effective in reducing the settlements caused by

tunnel excavation, from $w_{max}$ = -43 mm to −12 mm in the absence and the presence of the barrier, respectively, being able to reduce the measured settlement by about 70 % at the location of the line of piles. Additionally, the presence of the barrier proved to be effective in reducing the volume loss by approximately 56 % in the monitoring section interacting with it, being $V_L$ = 0.96-1.31 % in the presence of the barrier compared to $V_L$ = 2.60 % in *green field* conditions.

– the efficiency of the barrier was also evident for the *Aurelian Walls*, which experienced a settlement and a rotation reduction of about 45 % and 75 %, respectively, in the portion of the wall protected by the barrier.

A 2D FE back-analysis of the monitoring data was also carried out to provide an insight into the observed behaviour. The FE model accounted for the main activities of each working stage, considering both the absence and the presence of the embedded protective barrier consisting of a piled wall.

It has been shown that a fair agreement between the observed and computed settlements induced at the ground surface by conventional tunnelling could only be obtained if the grout injection effects were simulated by a volumetric expansion of the treated area. The magnitude and distribution of the volumetric strains induced by grout injection were calibrated to reproduce the ground surface heave observed during the grouting process, which had the major effect of inducing an increase in the horizontal effective stress close to the spring lines of the mini-tunnels. Once this change in effective stress was accounted for in the analyses, a plane-strain simulation of conventional excavation of the first tunnel was carried out using the force-based relaxation method. The simulation of the second tunnel was then carried out with the same parameters obtaining a fair agreement between the computed and observed settlement troughs at the end of the tunnels excavation. Such agreement could not have been obtained by ignoring the installation effects related to grout injections. This shows that when side operations such as the grout injections are simulated as wished-in-place in the analyses, i.e. they are simply activated by increasing the stiffness and strength properties of the treated area, the design predictions may not match the observed behaviour.

## CRediT authorship contribution statement

**Luca Masini:** Writing – original draft, Methodology, Investigation, Conceptualization. **Federico Bergamo:** Methodology, Investigation, Conceptualization. **Sebastiano Rampello:** Writing – review & editing, Supervision, Project administration, Methodology, Conceptualization.

## Declaration of competing interest

The authors declare that they have no known competing financial interests or personal relationships that could have appeared to influence the work reported in this paper.

## Acknowledgements

The Authors are indebted to Metro C ScPA and Mr. Eliano Romani for making available the monitoring data.

## Data availability

Data will be made available on request.

## References

Bai, Y., Yang, Z., Jiang, Z., 2014. Key protection techniques adopted and analysis of influence on adjacent buildings due to the Bund Tunnel construction. Tunn. Undergr. Space Technol. 41, 24–34.
Benz, T., Vermeer, P.A., Schwab, R., 2009. A small strain overlay model. Int. J. Numer. Anal. Meth. Geomech. 33, 25–44.
Bilotta, E., 2008. Use of diaphragm walls to mitigate ground movements induced by tunnelling. Géotechnique 58 (2), 143–155.
Bilotta, E., Taylor, R.N., 2005. Centrifuge modelling of tunnelling close to diaphragm wall. Int. J. Phys. Model. Geotech. 1, 25–41.
Brinkgreve, R.B.J., Engin, E., Swolfs, W.M., 2014. Plaxis 2D user manual. Plaxis BV, Delft, The Netherlands.
Burland, J.B., Wroth, C.P., 1974. Allowable and Differential Settlement of Structures, Including Damage and Soil Structure Interaction. In: Proceedings of the Conference on Settlement of Structures, pp. 611-654. Cambridge.
Croce, P., Flora, A., Modoni, G., 2014. Jet grouting, CRC Press. Taylor & Francis Group, Boca Raton, FL, p. 284.
Di Mariano, A., Gens, A., Gesto, J.M. and Schwartz, H. 2007. Ground deformation and mitigating measures associated with the excavation of the new Metro line. *In* Proceedings of the 14th European Confernce on Soil Mechanics and Geotechnical Engineering, Geotechnical Engineering in Urban Environments, Millpress Science Publisher, Rotterdam: The Netherlands, vol. 4, pp. 1901-1906.
Fantera, L., Rampello, S., Masini, L., 2016. A Mitigation Technique to Reduce Ground Settlements Induced by Tunnelling Using Diaphragm Walls. Procedia Eng. 158, 254–259.
Franza, A., Losacco, N., Ledesma, A., Viggiani, G.M.B., Jimenez, R., 2021. Protecting surface and buried structures from tunnelling using pile walls: a prediction model. Can. Geotech. J. 58 (10), 1590–1602. https://doi.org/10.1139/cgj-2020-0476.
Katzenbach, R., Leppla, S., Vogler, M., Seip, M. and Kurze, S. 2013. Soil-structure interaction of tunnels and superstructures during construction and service time. *In* Proceedings of the 11th International Conference on Modern Building Materials, Structures and Techniques, MBMST 2013, Procedia Engineering 57: 35-44.
Losacco, N., Romani, E., Viggiani, G.M.B., Di Mucci, G., 2019. Embedded Barriers as a Mitigation Measure for Tunnelling Induced Settlements: A Field Trial for the Line C in Rome. ITA-AITES World Tunnel Congress, Naples, Italy.
Mair, R.J., 2008. 46th Rankine Lecture: tunnelling and geotechnics: new horizons. Géotechnique 58 (9), 695–736.
Mair, R.J., Hight, D., 1994. Compensation grouting. World Tunnelling and Subsurface Excavation 7 (8).
Masini, L., Rampello, S., Romani, E., 2020. Performance of a Deep Excavation for the New Line C of Rome Underground. Lect. Notes Civ. Eng. 40, 575–582. https://doi.org/10.1007/978-3-030-21359-6_61.
Masini, L., Rampello, S., Viggiani, G.M.B., Soga, K., 2012. Experimental and numerical study of grout injections in silty soils. In: Proc. 7th International Symposium on Geotechnical Aspects of Underground Construction in Soft Ground, pp. 495–503.
Masini, L., Rampello, S., 2021. Predicted and observed behaviour of pre-installed barriers for the mitigation of tunnelling effects. Tunn. Undergr. Space Technol. 118, 104200.
Masini, L., Rampello, S., Soga, K., 2014. An approach to evaluate the efficiency of compensation grouting. Journal of Geotechnical and Geo-Environmental Engineering 140 (12), 04014073.
Masini, L., Gaudio, D., Rampello, S., Romani, E., 2021. Observed Performance of a Deep Excavation in the Historical Center of Rome. Journal of Geotech. Geoenviron. Eng., ASCE 147 (2), 05020015.
Masini, L., Rampello, S., Carloni, S. and Romani, E. 2019. Ground response to mini-tunnelling plus ground improvement in the historical city centre of Rome. Proc. of the WTC, 2019. ITA-AITES World Tunnel Congress. Naples, Italy.
Moh, Z.C., Huang, R.N. & Ju, D.H. 1996. Ground movements around tunnels in soft ground. Proc. Int. Symp. on Geotechnical Aspects of Underground Construction in Soft Ground, London, 725–730.
Mroueh, H., Shahrour, I., 2008. A simplified 3D model for tunnel construction using tunnel boring machines. Tunn. Undergr. Space Technol. 23, 38–45. https://doi.org/10.1016/j.tust.2006.11.008.
O'Reilly, M.P., New, B.M., 1982. Settlements above tunnels in the United Kingdom – Their magnitudes and prediction. Proc. Tunnelling '82 Symposium. 173–181, London.
Peck, R.B. 1969. Deep Excavation and Tunnelling in Soft Ground. State-of-the-Art Report. Proceedings of the 7th International Conference on Soil Mechanics and Foundation Engineering, Mexico, 1969, 225-290.
Potts, D.M., Zdravković, L., 2001. Finite Element Analysis in Geotechnical Engineering: Volume two – Application. Thomas Telford Publishing. https://doi.org/10.1680/feaigea.27831.
Rampello, S., Callisto, L., Viggiani, G., Soccodato, F.M., 2012. Evaluating the effects of tunnelling on historical buildings: the example of a new subway in Rome. Geomech. Tunnelling 5 (3), 254–262.
Rampello, S., Fantera, L., Masini, L., 2019. Efficiency of embedded barriers to mitigate tunnelling effects. Tunn. Undergr. Space Technol. 89, 109–124. https://doi.org/10.1016/j.tust.2019.03.027.
Rawlings, C.G., Hellawell, E.E., Kilkenney, M.W., 2000. Grouting for Ground Engineering. The Basingstoke Press, Hampshire, UK, CIRIA.
Ribacchi, R., Riccioni, R., 1977. Stato di sforzo e deformazione intorno ad una galleria circolare. Gallerie 5, 7–20.
Schanz, T., Vermeer, P.A., Bonnier, P.G., 1999. Hysteretic damping in a small-strain stiffness model. Proc. of the 10Th Int. Symp. on Numerical Models in Geomechanics.
Schikora, K., Fink, T., 1982. Berechnungsmethoden moderner bergmäannischer Bauweisen beim U-Bahn-Bau. Bauingenieur 57, 193–198.
Vermeer, P.A., Brinkgreve, R., 1993. Plaxis version 5 manual. A.A, Balkema, Rotterdam.
Vlachopoulos, N., Diederichs, M., 2009. Improved longitudinal displacement profiles for convergence confinement analysis of deep tunnels. Rock Mech Rock Eng 42, 131–146. https://doi.org/10.1007/s00603-009-0176-4.